Research Article

Fateh Ali*, Muhammad Zahid, M. Farmer, Nada Al Taisan*, Abdullah A. Faqihi, Basma Souayeh*, S. Suresh Kumar Raju, and Mir Waqas Alam

Hydrodynamic and sensitivity analysis of a polymeric calendering process for non-Newtonian fluids with temperature-dependent viscosity

https://doi.org/10.1515/phys-2025-0199
received April 11, 2025; accepted July 16, 2025

Abstract

Non-Newtonian fluids, particularly those with high viscosity and complex flow behavior, present unique challenges in manufacturing processes. The modeling of their flow dynamics is crucial to achieve the desired outcomes in industrial applications. This study aims to theoretically model and analyze the flow dynamics of the Eyring–Powell fluid under varying temperature conditions using lubrication approximation theory and perturbation method. To simplify the mathematical formulation of fluid flow motion, lubrication approximation theory is applied. Using a perturbation method, the dimensionless governing equations are solved to derive expressions for velocity, pressure gradient, and pressure distributions. Numerical integration is then used to calculate critical engineering parameters, such as power input and roll-separating force, offering practical insights for optimizing the manufacturing process. Additionally, using the response surface method, Nusselt number (Nu), sheet thickness $\left(\frac{H}{H_0}\right)$, and shear stress ($S_{xy}$), simulations were carried out to investigate the influence of variable viscoelastic parameters on the response functions (Nu, $\frac{H}{H_0}$, and S_{xy}). The virtuousness of appropriate of the empirical model is obvious based on the coefficient of determination (R^2) obtained from the analysis of variance. The findings reveal that the Weissenberg number, viscosity parameter, and Brinckmann number significantly influence velocity distribution, pressure profiles, power input, and roll-separating force, which are critical factors in the calendering process. Furthermore, the heat transfer rate shows an increase of approximately 5% with the rising values of the involved parameters, highlighting their significant influence on thermal performance. The coefficients of determination (R^2) rise by about 99% for all response parameters, indicating the empirical model's goodness of fit. These results provide valuable insights for engineers and researchers working on the calendering process of non-Newtonian fluids with complex rheological behavior, enabling better optimization of manufacturing processes and improved industrial outcomes.

Keywords: calendaring, non-Newtonian fluid, lubrication approximation theory, response surface methodology, analysis of variance, temperature-dependent viscosity

*** Corresponding author: Fateh Ali,** College of Mathematics and System Sciences, Xinjiang University, Urumqi, 830046, China, e-mail: fatehalirana@xju.edu.cn, fatehalirana47@gmail.com
*** Corresponding author: Nada Al Taisan,** Department of Physics, College of Science, King Faisal University, P. O. Box 400, Al-Ahsa, 31982, Saudi Arabia, e-mail: naltaisan@kfu.edu.sa
*** Corresponding author: Basma Souayeh,** Department of Physics, College of Science, King Faisal University, P. O. Box 400, Al-Ahsa, 31982, Saudi Arabia, e-mail: bsouayeh@kfu.edu.sa
Muhammad Zahid: Department of Mathematics, COMSATS University Islamabad, Abbottabad Campus, 22060, Abbottabad, Pakistan; Business School England, 252, 256 Romford Rd, London, E7 9HZ, United Kingdom, e-mail: drzahid@bse.ltd
M. Farmer: Business School England, 252, 256 Romford Rd, London, E7 9HZ, United Kingdom, e-mail: farmer@bse.ltd
Abdullah A. Faqihi: Department of Industrial Engineering, College of Engineering and Computer Science, Jazan University, P. O. Box 706, 45142, Jazan, Saudi Arabia, e-mail: afaqihi@jazanu.edu.sa
S. Suresh Kumar Raju: Department of Mathematics and Statistics, College of Science, King Faisal University, Al-Ahsa, 31982, Saudi Arabia, e-mail: ssurapuraju@kfu.edu.sa
Mir Waqas Alam: Department of Physics, College of Science, King Faisal University, P. O. Box 400, Al-Ahsa, 31982, Saudi Arabia, e-mail: wmir@kfu.edu.sa

Nomenclature

U	velocity of the rollers $\left(\frac{\mathrm{m}}{s}\right)$
H_0	half of the nip region

m	viscosity parameter
$R(m)$	radii of the roll
ρ	fluid density $\left(\frac{kg}{m^3}\right)$
λ	dimensionless leave off distance
We	perturb (small) parameter
Br	Brinckmann number
F	roll separation force
p_w	power input
$\frac{H}{H_0}$	final sheet thickness
$\frac{\mathrm{d}p}{\mathrm{d}x}$	pressure gradient
$p(x)$	pressure profile
$\theta(y)$	temperature profile

1 Introduction

A fluid's resistance to flow is highly influenced by temperature, pressure, and shear rate, all of which play crucial roles in determining the fluid's behavior. The kinetic energy of fluid particles generates temperature within the fluid, and higher temperatures can significantly alter fluid properties, with viscosity being particularly sensitive to temperature increases. In fluids with variable viscosity, viscosity responds rapidly to changes in temperature, resulting in alterations to the fluid's flow structure. Research on non-Newtonian fluids with temperature-dependent viscosity has been of significant interest for many years due to its importance in diverse industrial applications. This area encompasses a broad spectrum of phenomena relevant to processes such as oil drilling, food processing, and polymer manufacturing, where effective heat transfer is critical to operational efficiency and product quality. In these industrial settings, variations in viscosity can profoundly impact process efficiency and effectiveness. For example, understanding how viscosity varies with temperature can improve control over mixing uniformity and product consistency in fluid mixing applications. Thus, precise modeling and simulation of viscosity variations are essential for theoretical insights and for improving the design and efficiency of commercial operations, such as calendering [1].

The process of pulling molten polymer through the nip area in the middle of two sets of rotating rollers to create a sheet with a specific thickness is known as calendering. This process is integral to various industries, including textile, metal, paper, plastic, and tire manufacturing, where consistent material properties and controlled thickness are essential. Originating in the mid-nineteenth century, calendering technology was publicly demonstrated by inventors Edwin Chaffee and Charles Goodyear, marking a pivotal advancement in material processing. The first quantitative analysis of calendering, undertaken by [2] in 1938, introduced the application of lubrication approximation theory (LAT) within Newtonian hydrodynamics to address flow behavior at low Reynolds numbers, a regime typically encountered in calendering due to slow flow rates and narrow gaps. This analysis paved the way for more complex modeling approaches. Paslay's [3] work on the Maxwell model in calendering further advanced the theoretical framework, assuming Weissenberg numbers less than one to account for the viscoelastic response of polymeric fluids under flow. Experimental insights also contributed significantly to calendering science. In 1951, Bergen and Scott [4] conducted pioneering measurements of internal pressure distribution within the calendering system, providing critical empirical data for model validation. Gaskell's [5] study expanded upon this by offering the first theoretical analysis involving Bingham plastic and Newtonian fluids, noting that the interval width between rolls is negligible compared to the roll radii factor, which has considerable implications for flow stability and film uniformity. Thermal effects in calendering were subsequently addressed by Kiparissides and Vlachopoulos [6], who used a power-law fluid model to explore heat transfer dynamics. Their work involved solving the flow equations *via* the finite element method (FEM), showing strong agreement with experimental observations by Bergen and Scott, and highlighting the importance of temperature control in calendering applications. Tadmor and Gogos [7] and Brazinsky *et al.* [8] extended these analyses specifically for viscous power-law fluids commonly encountered in polymer processing, thus providing a comprehensive view of calendering flow behavior. Alston and Astill's [9] study advanced the computational methods used in calendering analysis by employing a hyperbolic tangent model, combined in the company of Gauss–Legendre cartesian and cascade repetition, to quantify spread height and peak roller pressure, as well as their interdependencies. Theoretical advancements in the coating process have been extensively discussed in textbooks; interested readers may refer to these sources for further details [7,10,11]. Later, in 1988, Zheng and Tanner [12] applied the Phan–Thien–Tanner model to further elucidate the viscoelastic flow characteristics within the calendering mechanism, underscoring the impact of non-Newtonian behavior on the procedure.

Newtonian and power-law fluids in calendering were thoroughly examined by Mitsoulis *et al.* in a two-dimensional, non-isothermal framework. Mitsoulis *et al.* [13] using the FEM without employing the LAT. Later,

Arcos *et al.* [14] explored the supremacy of various constants on sheet broadness in calendering using a temperature-dependent power-law fluid model, observing a 6.11% reduction in thickness compared to isothermal conditions. Sofou and Mitsoulis [15] extended this inquiry by simulating the finite sheet thickness calendering process for viscoplastic fluids modeled with the Herschel–Bulkley framework. A notable contribution by Hatzikiriakos [16] presented a numerical simulation focusing on the calendering of viscoplastic fluids, providing insights into material behavior under different calendering conditions. Arcos *et al.* [17] further advanced the understanding of calendering by employing a Newtonian fluid model that incorporated thermosensitive viscosity effects on sheet broadness. Within a separate investigation of non-isothermal flows in Casson fluids, Zahid *et al.* [18] addressed the complex thermal dynamics present in the calendering process. The work by Hernández *et al.* [19] examined a particular impact of pressure-dependent viscosity on sheet broadness at the exit of the calendering procedure, highlighting how pressure variations influence final product dimensions. Additionally, Arcos *et al.* [20] developed a theoretical model for calendering utilizing a more comprehensible Phan–Thien–Tanner essential equation beneath the lubrication approximation theory estimation. In investigating viscoelastic fluid dynamics, Ali *et al.* [21] scrutinize the effects of finitely extensible nonlinear elastic peterlin fluid (FENE-P) moisture in calendering, demonstrating significant viscoelastic influences on the process. Calcagno *et al.* [22] developed an analytical model for predicting pressure and tension profiles during calendering using Newtonian and power-law fluid assumptions. Their results aligned most closely with experimental findings when employing the Newtonian model. Most recently, Zahid *et al.* [23] presented a theoretical investigation on calendering with variable viscosity for third-grade model, analyzing how specific material properties influence the thickness of calendered sheets.

Most theoretical works in this dynamic research field concentrate on adhesive moisture; others are usually Newtonian. Numerous academics have included non-Newtonian vapors in their physically modeled issues, indicative of their widespread application in commercial settings. Here, theoretical investigation of non-Newtonian fluid dynamics is of primary interest [24]. A specific innumerable implementation of non-Newtonian in the technical, industrial, and commercial production sectors has increased interest in their study. Several authors have shown that non-Newtonian fluids apply to research [25]. Several studies have illustrated the various uses of non-Newtonian vapors. Several fluids collapse under this section, encompassing paper pulp, mayonnaise, cleaning agent, seashore, plastic melts, milk, and slurries. The Navier–Stokes identification can narrate the drizzle deportment of Newtonian fluids. Despite that, viscoelastic fluids' flow behavior with all of its essential qualities is not in a position to be sufficiently narrated by a unique equation. Consequently, scientists and academics have proposed several non-Newtonian constitutive models. The viscoelastic fluid, power-law fluid, Cassion fluid, distinctive class fluid imitation, Sisko fluid, FENE-P fluid, Oldroyd family's fluid, micropolar fluid, along with Eyring–Powell fluid, are a few examples of these patterns. We selected a specific Eyring–Powell fluid version, a non-Newtonian fluid imitation first presented among several fluid models [26,27]. This model performs better than previous viscoelastic fluid models in assorted areas. There are two main reasons why it offers many benefits. First, it uses the kinetic theory of object interactions instead of depending on the experimental formulas. Second, as is typical of Newtonian fluids, Eyring–Powell modeling responds to high and low shear rates. Researchers have talked a lot about the critical components of the Eyring–Powell fluid.

In the immediate years, there has been an extended use of experimental techniques to investigate the connections in the middle of free and response variables in complex systems. The hybrid statistical–mathematical approach known as response surface methodology (RSM) has gained significant traction among these methods. The primary objective of RSM is response optimization, which is particularly valuable for solving problems in heat transfer and fluid dynamics, as it aids in optimizing desired flow patterns. For instance, Darbari *et al.* [28] wore RSM to scrutinize a certain consequence of temperature and velocity on the standard Nusselt together with Reynolds numbers of nanofluids. Their study focused on nanofluids flowing through a straight, circular conduit under a steady thermal flux in the laminar regime. The RSM analysis revealed that temperature and velocity substantially impacted the dependent variables, with a notable interaction effect between these factors. As a result, RSM has become a widely adopted tool across various research domains for analyzing and optimizing complex interactions between multiple variables.

As far as we know and the scientific literature review, no attempt has yet been undertaken to analyze the calendering process using the Eyring–Powell model with viscosity temperature-dependent. Thus, the current work's goal is to ascertain how, throughout the calendering process, the fluid parameter influences the leave distance, power input, velocity, final sheet thickness, and other quantities of engineering interest.

An examination of the structure and content of the literature mentioned earlier reveals several critical observations:

- Numerous studies have explored the calendering process involving various non-Newtonian fluids, often assuming constant thermophysical properties. However, there remains a notable gap in research that explicitly addresses the impact of temperature-dependent viscosity, particularly in the context of Eyring–Powell fluids.
- A significant number of studies fail to comprehensively analyze key engineering characteristics, such as sheet thickness, Nusselt number, shear stress, roll/sheet separating force, and power transmitted from the roll to the fluid. These parameters are crucial for optimizing industrial processes and ensuring high-quality outcomes.
- Additionally, there is limited focus on the concurrent optimization of critical performance parameters, such as heat transfer rate, sheet thickness, and shear stress rate, which play a pivotal role in achieving efficient and effective manufacturing processes.

In light of these gaps identified through the literature review, the primary objectives of the present study are as follows:

- To construct a robust mathematical model for the calendering process using an Eyring–Powell fluid with temperature-dependent viscosity, incorporating Reynold's viscosity model to account for variable viscosity effects.
- To investigate the influence of temperature-dependent viscosity on the dynamics of the calendering process, emphasizing its implications for real-world applications.
- To examine the effects of pertinent parameters on critical engineering factors, including coating thickness, shear stress rate, heat transfer coefficient, roll/sheet separating force, and power transmitted from the roll to the fluid.
- To identify and address the limitations associated with achieving dual optimization goals of the maximizing the heat transfer rate while minimizing the shear stress rate through the application of advanced optimization techniques.

Comparison of existing studies on the calendering process was made using different non-Newtonian fluid models and contributions of the present study.

Author(s)	Fluid model	Process type	Limitations	Findings
Javed *et al.* [29]	Ellis fluid	Calendering	Did not consider temperature effects	Investigated coating performance at constant viscosity
Javed *et al.* [30]	Johnson–Segalman fluid	Calendering	Neglected magnetic field interactions	Did not consider variable viscosity
Abbas and Khaliq [31]	Cu–water nanofluid	Calendering	Did not consider RSM	Explored effects of different parameters on velocity and temperature, *etc.*
This study	Eyring–Powell fluid	Calendering	Ignore MHD and slip effects	Novelty: incorporates temperature-dependent viscosity with hybrid perturbation + RSM analysis for calendering process

2 Problem description and governing equations

The following presumptions are expressed:

- Figure 1 shows the calendering process sketch in which a non-Newtonian model's thin film separates two rolls.
- Since many materials used in calendering are frequently non-Newtonian, the Eyring–Powell model is considered to have temperature-dependent viscosity.
- The radius of each calendar is R, revolves with a persistent angular velocity ω in the same direction, provoking inside a linear velocity concerning its exterior designated by $U = \omega R$.
- Figure 1 shows a small separation region between calendars known as the nip area, with a gap length of $2H_0$.
- Certain roll surfaces occur concerning a sustained temperature T_0.
- Due to the symmetry of the physical model, we consider the upper side of this configuration only for convenience.

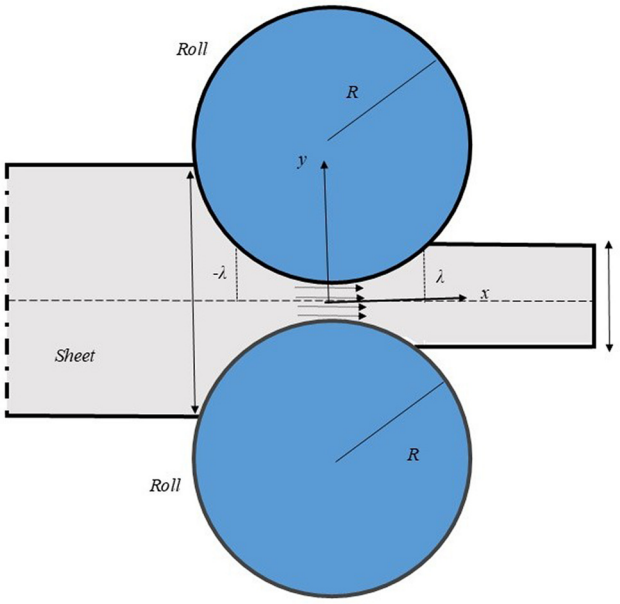

Figure 1: Illustrative depiction of the calendering procedure.

Without body forces, the momentum, mass, and energy equations are as follows [1,32]:

$$\nabla \cdot \mathbf{V} = 0, \tag{1}$$

$$\rho \frac{D\mathbf{V}}{Dt} = \mathrm{div}\boldsymbol{\tau} - \nabla\rho, \tag{2}$$

$$\rho C_{\mathrm{p}}\left(\frac{DT}{Dt}\right) = k\nabla^2 T + \boldsymbol{\tau} \cdot \nabla V, \tag{3}$$

where ρ corresponds to the constant fluid density, C_{p} represents the specific heat capacity, T represents the temperature profile, $\mathbf{V}$ denotes the velocity field, p signifies the pressure, k stands for the thermal conductivity, and $\boldsymbol{\tau}$ denotes the stress tensor.

The following is the material derivative:

$$\frac{D(.)}{Dt} = \frac{\partial(.)}{\partial t} + (\mathbf{V}\cdot\nabla)(.). \tag{4}$$

Scientists and engineers frequently reduce mathematical models to produce helpful approximations when working with complex physical systems. This procedure aims to improve comprehension of the physical system by emphasizing essential elements such as velocities, forces, fluxes, and other pertinent elements. We employ lubrication approximation theory in light of the aforementioned presumptions. The lubrication approximation theory indicates that the most significant dynamic events occur in the nip region, providing a basis for a thorough investigation.

The velocity profile of a balanced, incompressible, two-dimensional flow with laminar features can be noted as follows:

$$\mathbf{V} = [u(x,y), v(x,y)], \tag{5}$$

where a specific velocity component within the x- and y-directions are nominated by the variables $u(x,y)$, and $v(x,y)$, separately.

2.1 Rheological model

The viscoelastic Eyring–Powell model's description of the rheological characteristics is examined in this work. The following equations provide the Eyring–Powell model [33–35] in mathematical representation:

$$\tau = \mu\mathbf{A}_1 + \frac{1}{B}\frac{\sinh^{-1}\left(\frac{\sqrt{\mathrm{tr}(A_1)^2}}{2C}\right)}{\frac{\sqrt{\mathrm{tr}(A_1)^2}}{2}}\mathbf{A}_1, \tag{6}$$

where μ represents the viscosity; $\mathbf{A}_1$ denotes the primary Rivlin–Ericksen tensor; and B and C are the constants of the EP fluid version:

$$\mathbf{A}_1 = (\nabla\mathbf{V})^T + \nabla\mathbf{V}, \tag{7}$$

where $\nabla\mathbf{V}$ denotes the velocity gradient and is designated as

$$\nabla\mathbf{V} = \begin{bmatrix} \frac{\partial u}{\partial x} & \frac{\partial u}{\partial y} \\ \frac{\partial v}{\partial x} & \frac{\partial u}{\partial y} \end{bmatrix}. \tag{8}$$

With the use of Eqs. (5) and (6), the constituent appearance of the governing equations is written as follows:

$$\frac{\partial u}{\partial x} + \frac{\partial v}{\partial y} = 0, \tag{9}$$

$$\rho\left(u\frac{\partial u}{\partial x} + v\frac{\partial u}{\partial y}\right) = -\frac{\partial p}{\partial x} + \frac{\partial \tau_{xx}}{\partial x} + \frac{\partial \tau_{xy}}{\partial y}, \tag{10}$$

$$\rho\left(u\frac{\partial v}{\partial x} + v\frac{\partial v}{\partial y}\right) = -\frac{\partial p}{\partial y} + \frac{\partial \tau_{yx}}{\partial x} + \frac{\partial \tau_{yy}}{\partial y}, \tag{11}$$

$$\begin{aligned}\rho C_{\mathrm{p}}\left(u\frac{\partial T}{\partial x} + v\frac{\partial T}{\partial y}\right) = k\left[\frac{\partial^2 T}{\partial x^2} + \frac{\partial^2 T}{\partial y^2}\right] + \tau_{xx}\frac{\partial u}{\partial y} \\ + \tau_{xy}\left(\frac{\partial u}{\partial y} + \frac{\partial v}{\partial x}\right) + \tau_{yy}\frac{\partial v}{\partial y}.\end{aligned} \tag{12}$$

By applying the Taylor augmentation to the inverse hyperbolic expression in Eq. (6), we obtain the non-zero shear stress component in the simplified version as follows:

$$\tau_{xy} = \left(\mu + \frac{1}{\mathrm{BC}}\right)\frac{\partial u}{\partial y} - \frac{1}{6\ \mathrm{BC}^3}\left(\frac{\partial u}{\partial y}\right)^3. \tag{13}$$

The following are the boundary conditions (BCs) in the proportion configuration linked to Eqs. (10)–(12):

$$\begin{cases} y = 0 : \dfrac{\partial u}{\partial y} = 0 : \dfrac{\partial T}{\partial y} = 0, \\ y = h(x) : u = U : T = T_0. \end{cases} \tag{14}$$

For the $R > H_0$, the roll surface is approximately parallel and extends to any direction or in the $\pm x$ direction, from the nip. As a result, we conclude that the flow in the nip region is parallel.

The pressure, velocity, and fluid temperature profiles are represented by the letters p, u, v and T in Eqs. (9)–(12).

We do an order of magnitude study to quickly determine the typical temperature, pressure, and velocity scales. The following scales for y, x, as well as u changes should be identifiable.

$$y \sim H_0, \quad x \sim L_c, \quad u \sim U. \tag{15}$$

Considering a particular mass conservation identity, Eq. (1), as well as a certain connection outlined over Eq. (15), we conclude that

$$\frac{v_c}{U} \sim \frac{H_0}{L_c} \leq 1. \tag{16}$$

According to a specific connection exceeding the longitudinal predictable length, represented by $L_c = \sqrt{2RH_0}$, it is more significant than a particular disposition of immensity of a certain transverse speed v_c. Examine the tenable claim that a certain crucial dynamic affair occurred in the rolls nip region. Characteristic scales will be used in the next section to properly non-dimensionalize the system.

2.2 Non-dimensionalities, together with the lubrication approximation theory

Non-dimensional restriction can simplify complicated fluid flow problems and provide insightful information; they are highly significant in various scientific and engineering domains. Physical occurrences. This segment offers the dimensionless identities required to work through the non-isothermal calendering process. We identify the following non-dimensional variables based on the order of magnitude analysis from earlier [10]:

$$\begin{aligned} &\bar{u} = \frac{u}{U}, \quad \bar{y} = \frac{y}{H_0}, \quad \bar{x} = \frac{x}{\sqrt{RH_0}}, \quad \bar{v} = \frac{v}{U}\sqrt{\frac{R_0}{H_0}}, \\ &\bar{p} = \frac{\rho H_0^{\frac{3}{2}}}{\mu_0 U R^{\frac{1}{2}}}, \quad \bar{\mu} = \frac{\mu}{\mu_0}, \quad \bar{T} = \frac{T - T_0}{T_1 - T_0}. \end{aligned} \tag{17}$$

Eqs. (9)–(13) are modified to provide the two-dimensional equations in dimensionless form by applying Eq. (17):

$$\frac{\partial \bar{u}}{\partial \bar{x}} + \frac{\partial \bar{v}}{\partial \bar{y}} = 0, \tag{18}$$

$$\varepsilon \,\mathrm{Re}\left(u\frac{\partial u}{\partial x} + v\frac{\partial u}{\partial y}\right) = -\varepsilon\frac{\partial p}{\partial x} + \delta\frac{\partial \tau_{xx}}{\partial x} + \frac{\partial \tau_{xy}}{\partial x}, \tag{19}$$

$$\varepsilon^2 \,\mathrm{Re}\left(u\frac{\partial u}{\partial x} + v\frac{\partial u}{\partial y}\right) = -\frac{\partial p}{\partial y} + \delta\frac{\partial \tau_{yy}}{\partial y} + \delta^2\frac{\partial \tau_{xy}}{\partial x}, \tag{20}$$

$$\frac{\partial^2 \bar{T}}{\partial \bar{y}^2} + \mathrm{Br}\bar{\tau}_{xy}\frac{\partial \bar{u}}{\partial \bar{y}} = 0, \tag{21}$$

$$\bar{\tau}_{xy} = (\mu + \bar{N})\frac{\partial \bar{u}}{\partial \bar{y}} - \frac{1}{3}\bar{N}\beta\left(\frac{\partial u}{\partial y}\right)^3. \tag{22}$$

Because of Eq. (22), Eqs. (19) and (21) yield

$$\mu\frac{\partial^2 \bar{u}}{\partial \bar{y}^2} + \frac{\partial \mu}{\partial \bar{y}}\frac{\partial \bar{u}}{\partial \bar{y}} + \bar{N}\left(1 - \frac{1}{3}\beta\left(\frac{\partial \bar{u}}{\partial \bar{y}}\right)^2\right)\frac{\partial^2 \bar{u}}{\partial \bar{y}^2} = \frac{\mathrm{d}\bar{p}}{\mathrm{d}\bar{x}}, \tag{23}$$

$$\frac{\partial^2 \bar{T}}{\partial \bar{y}^2} + \mathrm{Br}(\mu + \bar{N})\left(\frac{\partial \bar{u}}{\partial \bar{y}}\right)^2 - \frac{1}{3}\bar{N}\beta\mathrm{Br}\left(\frac{\partial \bar{u}}{\partial \bar{y}}\right)^4 = 0. \tag{24}$$

The following are the relationships for the non-dimensional variables over Eq. (23) as well as (24):

$$\beta = \frac{U^2}{2C^2H_0^2}, \quad h = \pm(1 + x^2), \quad \mathrm{Br} = \mathrm{Pr} \times \mathrm{Ec}, \tag{25}$$

where Br is the Brickman number, an immeasurable quantity representing the viscous-to-inertial force ratio in a fluid flow system, and Pr along with Ec is the Prandtl together with Eckert numbers. Furthermore, it is explained as the sum of the Eckert and Prandtl numbers. The viscosity models and solution process are presented in the next section. For clarity, we remove the overbars for dimensionless variables in the equations for clarity.

3 Viscosity model

Unique patterns are selected to depict a specific fluid according to its viscosity. In particular, the viscosity is a function of the fluid's temperature, and the imitation, as mentioned earlier, is known as a specific Reynolds model.

3.1 Reynolds model

To describe a given Reynolds dummy, a dummy with fluctuating viscosity, we shall ascertain a particular viscosity worth in terms of temperature as follows:

$$\mu = e^{-MT}, \tag{26}$$

where (α is any constant) and $M = \alpha(T_1 - T_0)$. If We is a small perturbation parameter, then let $M = \mathrm{We}\ m$. Furthermore, a material parameter, m, illustrates how temperature affects the variable viscosity. With Taylor expansion, Eq. (26) is reduced to

$$\mu = 1 - \mathrm{We}\, mT(y), \quad \frac{\mathrm{d}\mu}{\mathrm{d}y} = -\mathrm{We}\, m\frac{\mathrm{d}T(y)}{\mathrm{d}y}. \tag{27}$$

Based on the previously described presumptions, the equation relating to motion and heat is defined as

$$\begin{aligned}(1 - \mathrm{We}\, mT(y))\frac{\mathrm{d}^2u(y)}{\mathrm{d}y^2} - \mathrm{We}\, m\frac{\mathrm{d}T(y)}{\mathrm{d}y}\frac{\mathrm{d}u(y)}{\mathrm{d}y} \\ + \mathrm{We}\, N\frac{\mathrm{d}^2u(y)}{\mathrm{d}y^2} - \frac{\mathrm{We}\, N\beta}{3}\left(\frac{\mathrm{d}u(y)}{\mathrm{d}y}\right)^2\frac{\mathrm{d}^2u(y)}{\mathrm{d}y^2} = \frac{\mathrm{d}p}{\mathrm{d}x},\end{aligned} \tag{28}$$

$$\begin{aligned}\frac{\mathrm{d}^2T(y)}{\mathrm{d}y^2} + \mathrm{Br}(1 - \mathrm{We}\, mT(y))\left(\frac{\mathrm{d}u(y)}{\mathrm{d}y}\right)^2 \\ + \mathrm{BrWe}\, N\left(\frac{\mathrm{d}u(y)}{\mathrm{d}y}\right)^2 - \frac{\mathrm{BrWe}\, N\beta}{3}\left(\frac{\mathrm{d}u(y)}{\mathrm{d}y}\right)^4 = 0.\end{aligned} \tag{29}$$

BCs are [10]

$$\begin{cases} y = 0 : \dfrac{\partial u}{\partial y} = 0 : \dfrac{\partial \theta}{\partial y} = 0, \\ y = h(x) = x^2 + 1 : u = 1 : \theta = 0. \end{cases} \tag{30}$$

The expression for flow rate in dimensionless form, which will help to find the value of pressure gradient, can be corresponded in the formation as [10]:

$$Q = 1 + \lambda^2 = \int_0^{h(x)} u(y)\mathrm{d}y. \tag{31}$$

The approach of Eq. (28) along with (29) represents the prominent lubrication estimation [17] for Eyring–Powell fluid accompanied by thermosensitive viscosity. It must be esteemed that these identities are coupled and nonlinear. So, in the following section, we prevail the proportionate velocity, pressure gradient, pressure, and temperature profiles by solving Eqs. (28) and (29) with the help of BCs given in Eq. (30) using the perturbation method.

4 Asymptotic solution for We ≪ 1

To find the sheet thickness, pressure, detachment point, temperature distribution, and dimensionless velocity profile, Eqs. (28) and (29) have no exact solution; we try to determine an asymptotic solution, using We as the perturbation parameter and applying the regular perturbation method. For $We \ll 1$, one can take

$$u(y, x) = u_0(y, x) + \mathrm{We}\ u_1(y, x) + \mathrm{We}^2\ u_2(y, x) + \dots, \tag{32}$$

$$\frac{\mathrm{d}p}{\mathrm{d}x} = \frac{\mathrm{d}p_0}{\mathrm{d}x} + \mathrm{We}\frac{\mathrm{d}p_1}{\mathrm{d}x} + \mathrm{We}^2\frac{\mathrm{d}p_2}{\mathrm{d}x} + \dots, \tag{33}$$

$$p(x) = p_0(x) + \mathrm{We}\, p_1(x) + \mathrm{We}^2\ p_2(x) + \dots, \tag{34}$$

$$\theta = \theta_0 + \mathrm{We}\, \theta_1 + \mathrm{We}^2\, \theta_2 + \dots, \tag{35}$$

$$\lambda = \lambda_0 + \mathrm{We}\, \lambda_1 + \mathrm{We}^2\, \lambda_2 + \dots, \tag{36}$$

where the leading-order solutions u_0, p_0, $\frac{\mathrm{d}p_0}{\mathrm{d}x}$ and λ_0 denote the Newtonian case [10], and the correction up to first-order terms is represented by u_1, p_1, $\frac{\mathrm{d}p_1}{\mathrm{d}x}$ and λ_1, which includes the non-Newtonian effect's contribution. where $h(x) = x^2 + 1$, by equating the coefficients of We^0 and We^1, we may derive the series of the boundary value problems by expanding Eq. (28). The following subsection discusses zeroth together with first-order problems and their solutions.

4.1 Zero-order problem and its solution

The first-order partition value dilemma

$$\frac{\mathrm{d}^2}{\mathrm{d}y^2}u_0(y) = \varepsilon\frac{\mathrm{d}p_0}{\mathrm{d}x}. \tag{37}$$

BCs are

$$\begin{cases} y = 0 : \dfrac{\partial u_0}{\partial y} = 0, \\ y = h(x) = x^2 + 1 : u_0 = 1. \end{cases} \tag{38}$$

The solution of Eq. (37) with help of BCs given in Eq. (38) is as follows:

$$u_0(y) = \frac{1}{2}\varepsilon\frac{\mathrm{d}p_0}{\mathrm{d}x}(y^2 - h^2) + 1. \tag{39}$$

The zeroth-order pressure gradient is as follows:

$$\frac{\mathrm{d}p_0}{\mathrm{d}x} = -\frac{3(\lambda_0^2 - x^2)}{\varepsilon(x^2 + 1)^3}. \tag{40}$$

From the aforementioned equation, the zero-order pressure is

$$p_0(x) = \frac{9\pi\lambda_0^4 + 18\arctan(\lambda_0)\lambda_0^4 + 6\pi\lambda_0^2 + 12\arctan(\lambda_0)\lambda_0^2 + 18\lambda_0^3 - 3\pi - 6\arctan(\lambda_0) + 6\lambda_0}{16\varepsilon\lambda_0^2 + 16\varepsilon}. \tag{41}$$

The exceeding mathematical form is uncoordinated in λ_0. It is not conceivable to perceive it, which requires a solution for which a logarithmic algorithm exclaims the Newton–Raphson method is initiate with predefined precision, so the approximate solution is

$$\lambda_0 = 0.47512. \tag{42}$$

For this value of λ_0, the sheet thickness to most minor gap compass proportion is capable of to 1.226, which is similar to Middleman [10].

4.2 First-order complication and its emulsion

The first-order boundary value obstacle

$$\frac{d^2}{d^2y}u_1(y) - m\theta_0(y)\left(\frac{d^2}{d^2y}u_0(y)\right) - m\left(\frac{d}{dy}\theta_0(y)\right)\left(\frac{d}{dy}u_0(y)\right) + A\left(\frac{d^2}{dy^2}u_0(y)\right) - \frac{A\beta\left(\frac{d}{dy}u_0(y)\right)^2\left(\frac{d^2}{dy^2}u_0(y)\right)}{3} = \varepsilon\frac{dp_1}{dx}. \tag{43}$$

BCs [10] are

$$\begin{cases} y = 0 : \dfrac{\partial u_1}{\partial y} = 0 : \dfrac{\partial \theta_1}{\partial y} = 0, \\ y = h(x) = x^2 + 1 : u_1 = 0 : \theta_1 = 0. \end{cases} \tag{44}$$

The solution of Eq. (43) with aforementioned BCs is

$$u_1(y) = \frac{3(h-y)(h+y)}{4(x^2+1)^9}\left\{\begin{array}{l} \left(-\dfrac{2\varepsilon P_1 x^{18}}{3} - 6\varepsilon P_1 x^{16} + \left(-24\varepsilon P_1 + 2A - \dfrac{3m\mathrm{Br}}{2}\right)x^{14} + \left(\left(-2A + \dfrac{9m\mathrm{Br}}{2}\right)\lambda 0^2 - \right.\right. \\ \left.\left. 56\varepsilon P_1 - 6m\mathrm{Br} + 12A\right)x^{12} + \\ \left(-\dfrac{9\lambda 0^4 m\mathrm{Br}}{2} + (18m\mathrm{Br} - 12A)\lambda 0^2 - 84\varepsilon P_1 - 9m\mathrm{Br} + 30A\right)x^{10} + \\ \left(\dfrac{3\mathrm{Br}\lambda 0^6 m}{2} - 18\lambda 0^4 m\mathrm{Br} + (27m\mathrm{Br} - 30A)\lambda 0^2 - 84\varepsilon P_1 - 6m\mathrm{Br} + 40A\right)x^8 + \\ \left(\begin{array}{l} 6\mathrm{Br}\lambda 0^6 m - 27\lambda 0^4 m\mathrm{Br} + (18m\mathrm{Br} - 40A)\lambda 0^2 + \dfrac{m(h^4 + h^2y^2 + y^4 - 3)\mathrm{Br}}{2} + \\ (-\beta h^2 - \beta y^2 + 30)A - 56\varepsilon P_1 \end{array}\right)x^6 + \\ \left(\begin{array}{l} 9\mathrm{Br}\lambda 0^6 m - 18\lambda 0^4 m\mathrm{Br} + \left(-\dfrac{3m(h^4 + h^2y^2 + y^4 - 3)\mathrm{Br}}{2} + \right. \\ \left. 3A(\beta h^2 + \beta y^2 - 10)\right)\lambda 0^2 \\ -24\varepsilon P_1 + 12A \end{array}\right)x^4 + \\ \left(\begin{array}{l} 6\mathrm{Br}\lambda 0^6 m + \left(\dfrac{3m(h^4 + h^2y^2 + y^4 - 3)\mathrm{Br}}{2} - \right. \\ \left. 3A\beta(h^2 + y^2)\right)\lambda 0^4 \\ -12A\lambda 0^2 - 6\varepsilon P_1 + 2A \end{array}\right)x^2 + \\ \left(-\dfrac{m(h^4 + h^2y^2 + y^4 - 3)\mathrm{Br}}{2} + A\beta(h^2 + y^2)\lambda 0^6 - 2A\lambda 0^2 - \dfrac{2\varepsilon P_1}{3}\right) \end{array}\right\}. \tag{45}$$

The aforementioned identity requires an unrevealed pressure gradient $\frac{dp_1}{dx}$, and it can be procured as defined in a zero-order solution. Due to complex and lengthy expressions, equations are not displayed here.

5 Temperature distribution

We are now using the velocity distribution in Eq. (29), and with the help of Eq. (30), we obtain the following system of ordinary problems for the temperature profile.

5.1 Zero-order problem and its solution

$$\frac{d^2}{dy^2}T_0(y) = -\mathrm{Br}\left(\frac{d}{dy}u_0(y)\right)^2. \tag{46}$$

BCs are

$$\begin{cases} y = 0 : \dfrac{\partial \theta_0}{\partial y} = 0, \\ y = h(x) = x^2 + 1 : \theta_0 = 0. \end{cases} \tag{47}$$

Solution is

$$T_0(y) = \frac{3(-\lambda 0 + x)^2(\lambda 0 + x)^2(x^2 + y + 1)(x^2 - y + 1)(x^4 + 2x^2 + y^2 + 1)\mathrm{Br}}{4(x^2 + 1)^6}. \tag{48}$$

5.2 First-order problem

$$\begin{aligned}&\frac{\mathrm{d}^2}{\mathrm{d}y^2}\theta_1(y) + 2\mathrm{Br}\left(\frac{\mathrm{d}}{\mathrm{d}y}u_0(y)\right)\left(\frac{\mathrm{d}}{\mathrm{d}y}u_1(y)\right)\\ &- \mathrm{Br}m\theta_0(y)\left(\frac{\mathrm{d}}{\mathrm{d}y}u_0(y)\right)^2\\ &+ \mathrm{Br}\gamma\left(\frac{\mathrm{d}}{\mathrm{d}y}u_0(y)\right)^2 - \frac{\mathrm{Br}\gamma\beta\left(\frac{\mathrm{d}}{\mathrm{d}y}u_0(y)\right)^4}{3} = 0.\end{aligned} \tag{49}$$

BCs are

$$\begin{cases} y = 0 : \dfrac{\partial\theta_1}{\partial y} = 0, \\ y = h(x) = x^2 + 1 : \theta_1 = 0. \end{cases} \tag{50}$$

The expression for the first-order temperature is not presented here due to its large size. However, the solution to the first-order problem can be obtained by combining the zero-order and first-order approximations for the velocity, temperature profile, pressure gradient, and pressure distribution. Similarly, the detachment point and other engineering quantities are calculated using the numerical algorithm presented in Tables 16 and 17. Next, we will present the mathematical expression for the operational variable.

6 Operating variables

All other significant values can be easily obtained after determining the expressions for velocity, pressure gradient, and pressure distribution. These calculations are made for a particular engineering operating variable.

It is specified that a given roll-separating force F [10,29] is

$$F = \int_{-\infty}^{\lambda} P(x)\mathrm{d}x, \tag{51}$$

where $F = \frac{\bar{F}H_0}{\mu URW}$, $\bar{F}$ is a given dimensional roll-separating force per unit broadness W.

A calculation of the power transferred [29] to the fluid by roll involves integrating the result of the roll's surface spread over its surface, which is acquired by establishing the shear stress:

$$P_w = \int_{-\infty}^{\lambda} \tau_{xy}(x, 1)\mathrm{d}x, \tag{52}$$

where $P_w = \frac{\bar{P}}{\mu WU^2}$ is a particular dimensionless power and $\tau_{xy} = \frac{\bar{\tau}_{xy}H_0}{\mu U}$ is the dimensionless stress tensor.

7 RSM

The RSM-based statistical approach has been presented to ascertain the relative contributions of independent and dependent components. Operate a miniature numeral of planned experiments; RSM is a strategy for creating models, conducting tests, assessing abundant elements' influence, and regulating the ideal circumstances for desired answers. RSM is useful in illustrating the correspondence between a designated set of feed-in variables, a particular response over a defined region of interest, and the input values that will result in a maximum or minimum response. Today, RSM is utilized in many different domains and applications, including the biological, clinical, and social sciences, in addition to the physical and engineering sciences, where it was first established to identify ideal operating conditions for the chemical industry. It generates a link between input factors and output responses using analytical and numerical simulations. Two input variables are the We and m, and three response variables are the Nu, $\frac{H}{H_0}$, and S_{xy}. Here are the model's specifications:

$$\text{Responses} = \beta_0 + \beta_i x_i + \sum_{i=1}^{3}\beta_i x_i^2 + \sum_{i=1}^{3}\beta_i\beta_j x_i x_j, \tag{53}$$

where the physical components are x_i and x_j, and the residual and the regression variables are β_0, β_1, and β_3. Both linear and quadratic effects are included in the generic regression model that is displayedpreviously. There are 13 runs in the experimental design. Response variables are documented and situated on the coded values.

A specific central composite design (CCD) is the preponderance well-received of the second-order models employed by RSM. In 1951, Box and Wilson put out the idea. The published literature suggests using a three-level, face-centered CCD inside a particular RSM framework. Full replication is used, which includes factors at the medium (0), high (1), and low (−1) levels of specific specified parameters in the innovative composition.

Table 1: Parameters with their symbols and levels

Codes	Variables	Level		
		Low (−1)	Intermediate (0)	High (+1)
A	We	0.10	0.50	0.90
B	m	0.50	2.50	4.50

A particular investigational design and CCD-RSM succession proposed the combined scurry, displayed in Table 1 with the 13 numerical runs utilizing CFD Nu.

7.1 Analysis of variance (ANOVA)

Table 2 lists a particular result of specific numerical tests (Nu, $\frac{H}{H_0}$, and S_{xy}). Regression analysis has been utilized to construct mathematical models. The fitted regression models were evaluated for suitability and accuracy using the ANOVA and sequential f-test. The means of multiple groups are compared using the statistical technique known as ANOVA. Fisher first introduced it, consisting of standard statistical metrics that filtered out models to identify the most suited for unnecessary words.

Tables 3–5 display the ANOVA results, which are utilized to identify the correlations between the independent input components and the Nu, $\frac{H}{H_0}$, and S_{xy}. The result variable for various combinations of the input values is calculated in a series of test runs to estimate the model coefficients. Regression analysis techniques are then used to identify the best-fit coefficient values through data analysis. Various statistical measures, such as a given F-value, a specific p-value, a certain degree of freedom (DOF), a particular mean sum of squares (MS), along with a specific sum of squares (SS), are employed to calculate the magnitude to which the model matches the figures successfully. It has been determined through the computation of p-values that the three factors receiving investigation significantly influence both replies, with the p-value being below 0.0001.

Table 2: Experimental outline and responses

Std	Run	Space type	Factor 1 A: We	Factor 2 B: m	Response 1 Nusselt number	Response 2 Sheet thickness	Response 3 Shear stress
6	1	Axial	0.9	2.5	−0.116348	1.23242	−0.4996
13	2	Center	0.5	2.5	−0.0986044	1.22944	−0.42778
7	3	Axial	0.5	0.5	−0.108189	1.236	−0.45664
8	4	Axial	0.5	4.5	−0.0885624	1.22264	−0.4
11	5	Center	0.5	2.5	−0.0986044	1.22944	−0.42778
10	6	Center	0.5	2.5	−0.0986044	1.22944	−0.42778
5	7	Axial	0.1	2.5	−0.0808603	1.22648	−0.35635
2	8	Factorial	0.9	0.5	−0.133602	1.24438	−0.55987
12	9	Center	0.5	2.5	−0.0986044	1.22944	−0.42778
3	10	Factorial	0.1	4.5	−0.0788519	1.22512	−0.35138
1	11	Factorial	0.1	0.5	−0.0827773	1.22777	−0.36119
4	12	Factorial	0.9	4.5	−0.0982729	1.22018	−0.44461
9	13	Center	0.5	2.5	−0.0986044	1.22944	−0.42778

Table 3: ANOVA for quadratic model for Nusselt number

Source	Sum of squares	Df	Mean square	f-value	p-value	
Model	0.0027	5	0.0005	84515.75	<0.0001	Significant
A-We	0.0019	1	0.0019	2.929×10^{05}	<0.0001	
B-m	0.0006	1	0.0006	90847.65	<0.0001	
AB	0.0002	1	0.0002	38761.66	<0.0001	
A^2	0.0000	1	0.0000	0.0000	1.0000	
B^2	1.441×10^{-07}	1	1.441×10^{-07}	22.66	0.0021	
Residual	4.452×10^{-08}	7	6.360×10^{-09}			
Lack of fit	4.452×10^{-08}	3	1.484×10^{-08}			
Pure error	0.0000	4	0.0000			
Cor total	0.0027	12	0.0005			

Table 4: ANOVA for quadratic model for sheet thickness

Source	Sum of squares	df	Mean square	*F*-value	*p*-value	
Model	0.0004	5	0.0001	96017.21	<0.0001	Significant
A-We	0.0001	1	0.0001	56727.36	<0.0001	
B-m	0.0003	1	0.0003	2.959×10^{05}	<0.0001	
AB	0.0001	1	0.0001	1.274×10^{05}	<0.0001	
A^2	1.639×10^{-09}	1	1.639×10^{-09}	1.80	0.2217	
B^2	2.967×10^{-08}	1	2.967×10^{-08}	32.56	0.0007	
Residual	6.379×10^{-09}	7	9.112×10^{-10}			
Lack of fit	6.379×10^{-09}	3	2.126×10^{-09}			
Pure error	0.0000	4	0.0000			
Cor total	0.0004	12				

Table 5: ANOVA for 2FI model for shear stress

Source	Sum of squares	Df	Mean square	*F*-value	*p*-value	
Model	0.0398	3	0.0133	6205.91	<0.0001	Significant
A-We	0.0316	1	0.0316	14747.34	<0.0001	
B-m	0.0055	1	0.0055	2571.42	<0.0001	
AB	0.0028	1	0.0028	1298.97	<0.0001	
Residual	0.0000	9	2.140×10^{-06}			
Lack of fit	0.0000	5	3.852×10^{-06}			
Pure error	0.0000	4	0.0000			
Cor total	0.0399	12				

The quality of fit is evaluated by considering the dependence on multiple indices. A specific *p*-value for each fitted dummy is slighter than 0.0001 for the initial deficiency of fit. Second, the model's ability to account for response variation is demonstrated R^2 and modified R^2. The R^2 value in a regression model is a particular percentage of discrepancy in a particular dependent variable that can be spell out by the independent variables. When the R^2 value is higher, it stipulates that a specific model of regression fits the data well. In this case, the R^2 value is measured at about 99% for all response variables; this implies that this model is appropriate for determining the response function values.

A specific accuracy of a given constructed regression model is validated by examining the ANOVA, refer to Tables 3–5. By evaluating *p* and *F* values, the discrepancy in a given data and the dummy significance are determined. The detailed discussion about *p* and *f* values for the Nusselt number is that the Forecast R^2 of 0.9998 is in coherent agreement with the conformed R^2 of 1.0000; *i.e.*, the difference is slighter than 0.2. Adeq precision standard the signal-to-noise ratio. A ratio greater than 4 is desirable. The ratio 1012.741 signifies an adequate signal. This paradigm can facilitate map-reading inside the design space. The model *F*-value of 84515.75 designates the model's significance. It is approximately 0.01% likely that an *F*-value of this size would result from random noise. *P*-values slighter than 0.0500 designates statistical significance for the model terms. *A*, *B*, *AB*, along with B^2, are the dominant terms in the model. Values beyond 0.1000 recommend that the model terms lack significance. Model depletion may amplify your model if numerous inconsequential terms are contemporary, except those mandatories for hierarchical support. The summary of fit data for all replies are present in Tables 6–8.

For sheet thickness, the predicted R^2 of 0.9999 is in practicable concurrence with a particular adjusted R^2 of

Table 7: Fit statistics

Std. dev.	0.0000	R^2	1.0000
Mean	1.23	Adjusted R^2	1.0000
C.V. %	0.0025	Predicted R^2	0.9999
		Adeq precision	1179.1611

Table 6: Fit statistics summary

Std. dev.	0.0001	R^2	1.0000
Mean	−0.0985	Adjusted R^2	1.0000
C.V. %	0.0810	Predicted R^2	0.9998
		Adeq precision	1012.7410

Table 8: Fit statistics

Std. dev.	0.0015	R^2	0.9995
Mean	−0.4283	Adjusted R^2	0.9994
C.V. %	0.3415	Predicted R^2	0.9978
		Adeq precision	253.3947

1.0000; *i.e.*, the differentiation is slighter than 0.2. Adeq precision estimates the signal-to-noise ratio. A ratio more substantial than 4 is recommendable. The ratio 1179.161 suggested a requisite signal. The design area can be traverse with the help of this dummy. The model *F*-value of 96017.21 designates that a specific dummy is notable. The prospect of obtaining an *F*-value of this enormousness due to random clamor is about 0.01%. *P*-values beneath 0.0500 signify that the model terms are scientifically notable. *A*, *B*, *AB*, and B^2 are dominant terms in the model. Values beyond 0.1000 manifest that the model terms lack significance. Model depletion may amplify your model if numerous irrelevant words are present (excluding those necessary for hierarchy support).

For shear stress, the predicted R^2 of 0.9978 is in practicable concurrence with the adjusted R^2 of 0.9994; *i.e.*, the distinction is slighter than 0.2. Adeq precision quantifies the signal-to-noise ratio. A proportion over 4 is preferable. The ratio of 253.395 is evidence of an ample signal. This model is pertinent for traversing the design interval. The model *F*-value of 6205.91 stipulates that the model is significant. The probability of an *F*-value of this

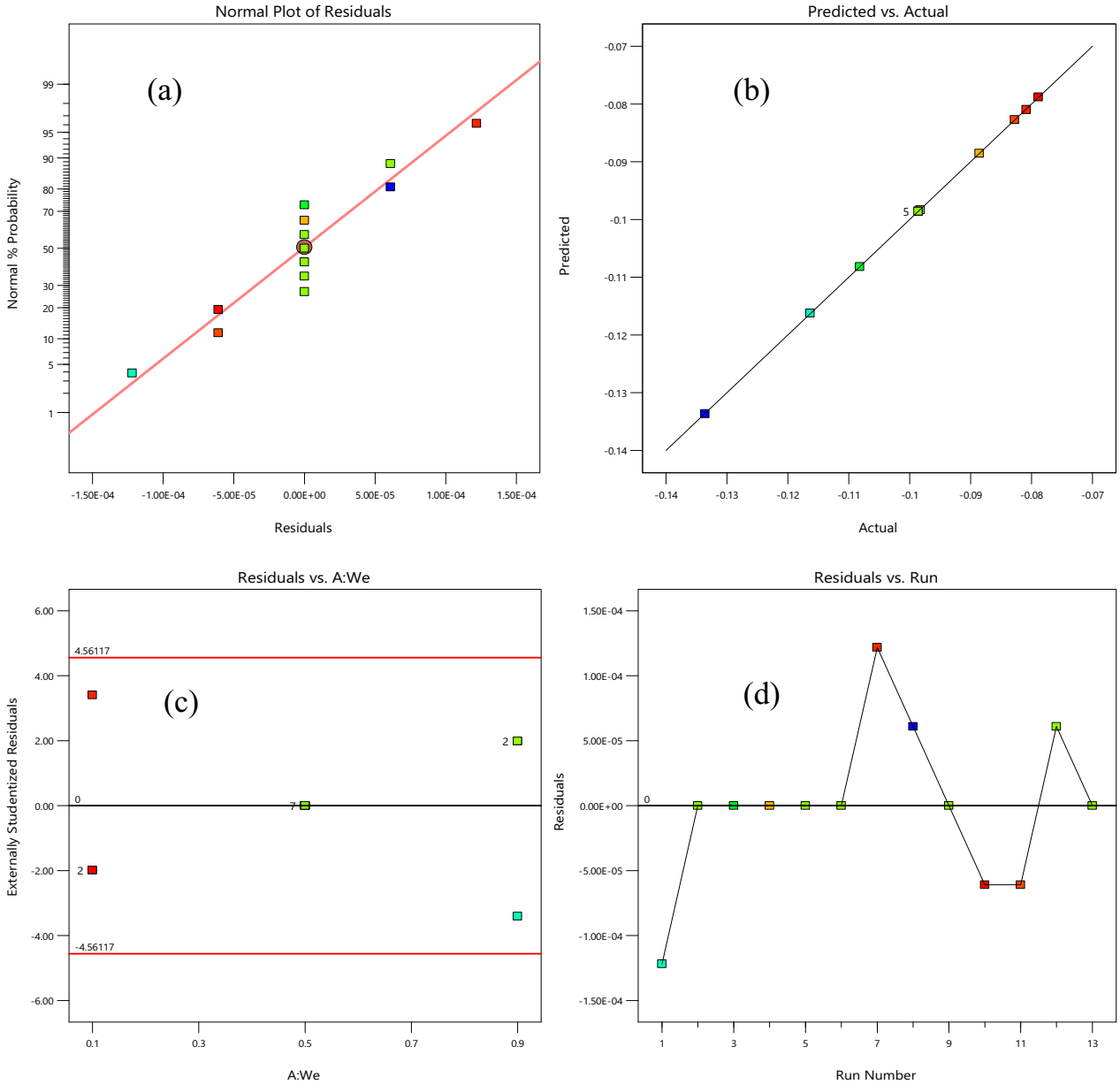

Figure 2: Residual plots for Nu: (a) normal probability, (b) goodness of fit, (c) studentized residuals against predicted, and (d) studentized residuals against the run number.

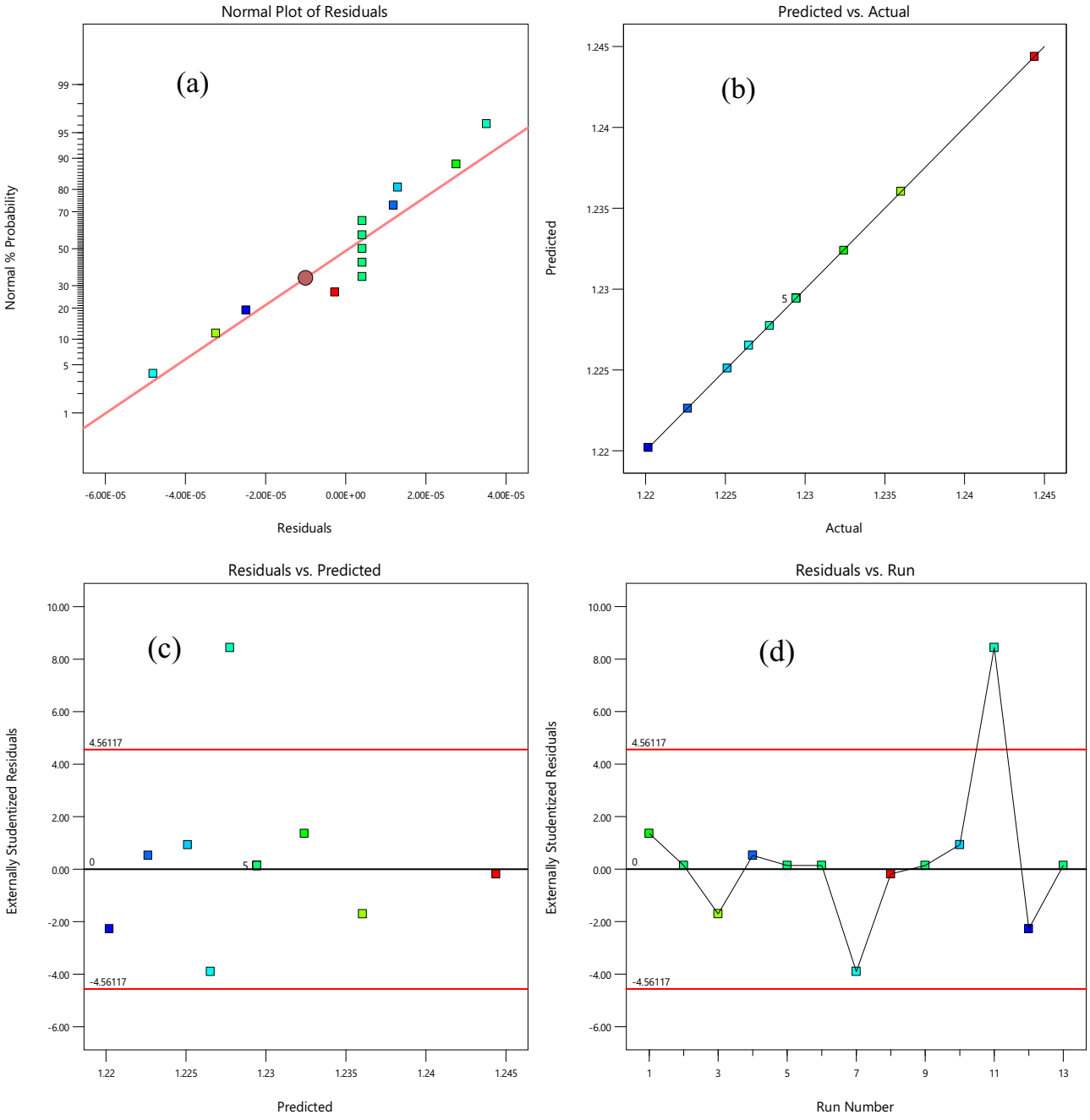

Figure 3: Residual plots for sheet thickness: (a) normal probability, (b) goodness of fit, (c) studentized residuals against predicted, and (d) studentized residuals against run number.

enormousness arising from random noise is about 0.01%. *P*-values below 0.0500 signify that the model terms are statistically significant. *A*, *B*, and *AB* are dominant terms in the model. Values beyond 0.1000 signify that the model terms lack modification. Model reduction may enhance your model if numerous inconsequential terms are present, except those necessary for hierarchical support.

7.2 Regression models of responses

Figures 2–4, independently, show the surplus and normal probability charts for Nu, $\frac{H}{H_0}$, and S_{xy}. These charts show two often-used diagnostic representations used to examine a regression model's hypotheses. The frequency distribution shows a steady linear tendency, supporting the

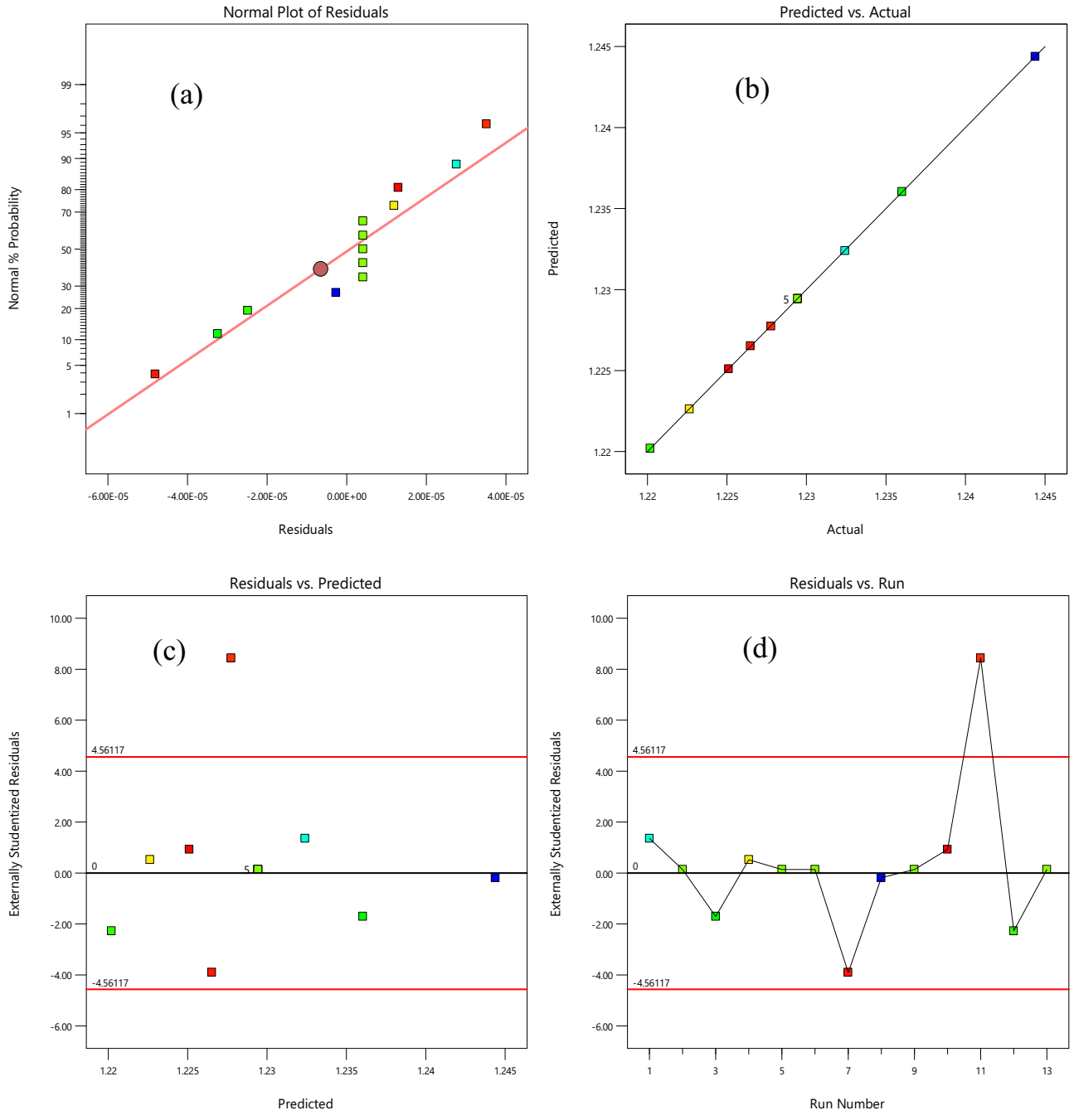

Figure 4: Residual plots for share stress: (a) normal probability, (b) goodness of fit, (c) studentized residuals against predicted, and (d) studentized residuals against run number.

hypothesis that the errors have a normal distribution. The interconnection between a particular anticipated and actual values exhibits a specific model's degree of validity and fit. A specific residual for Nu as well $\frac{H}{H_0}$ is almost exactly a straight line, which leads one to believe that the inaccuracy has standard dissemination.

The forecast values *vs* particular actual ones for Nu, $\frac{H}{H_0}$, as well as S_{xy} are shown in Figures 2(b) and 3(b) and and 4(b). These graphs show that the residuals nearly match an aligned line, indicating that a particular regression dummy correctly predicted the actual values. Also, a specific actual value (design points) has been contrasting to the expected

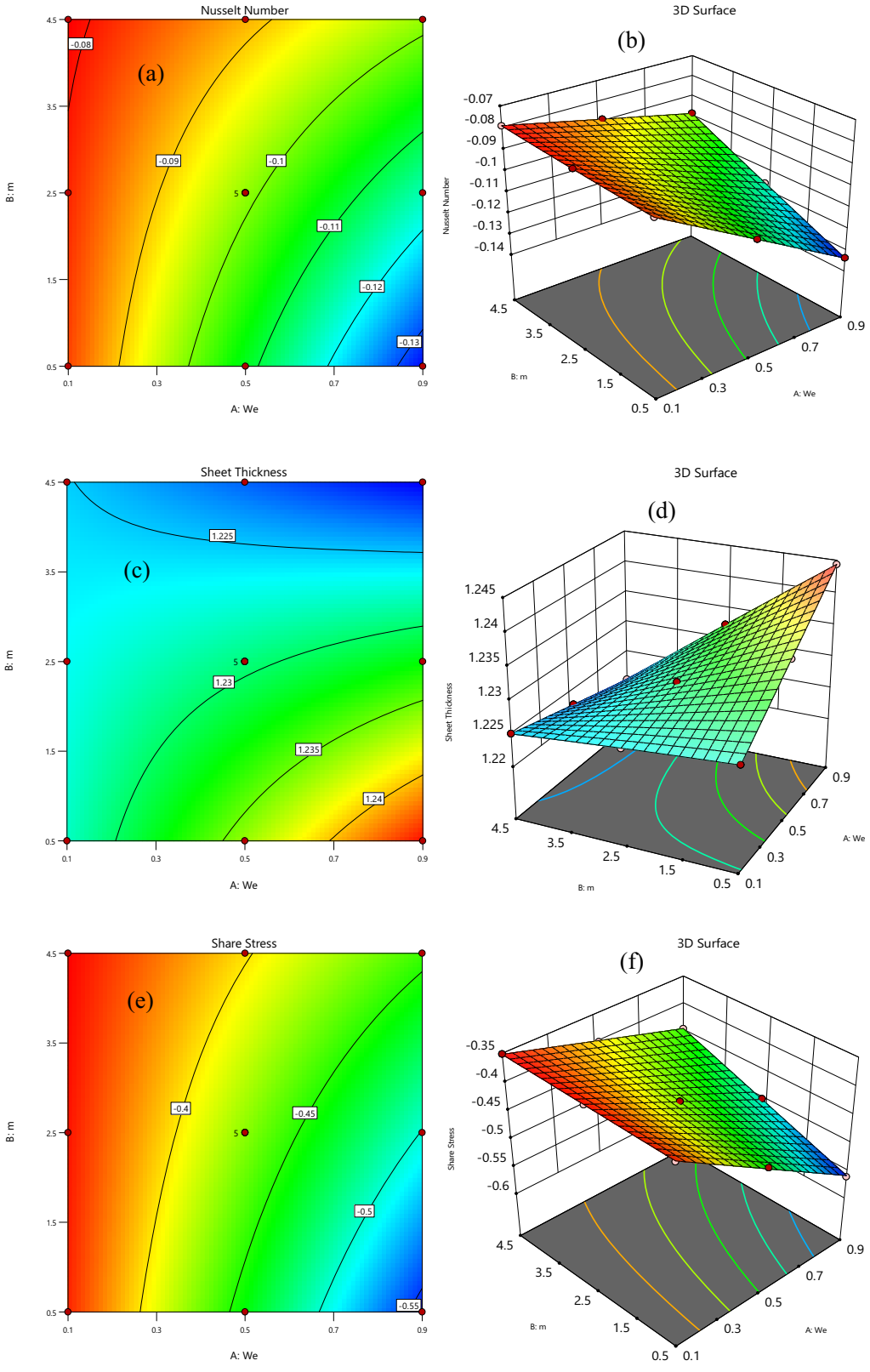

Figure 5: Contour and 3D surface response plot of Nu, $\frac{H}{H_0}$, and S_{xy}.

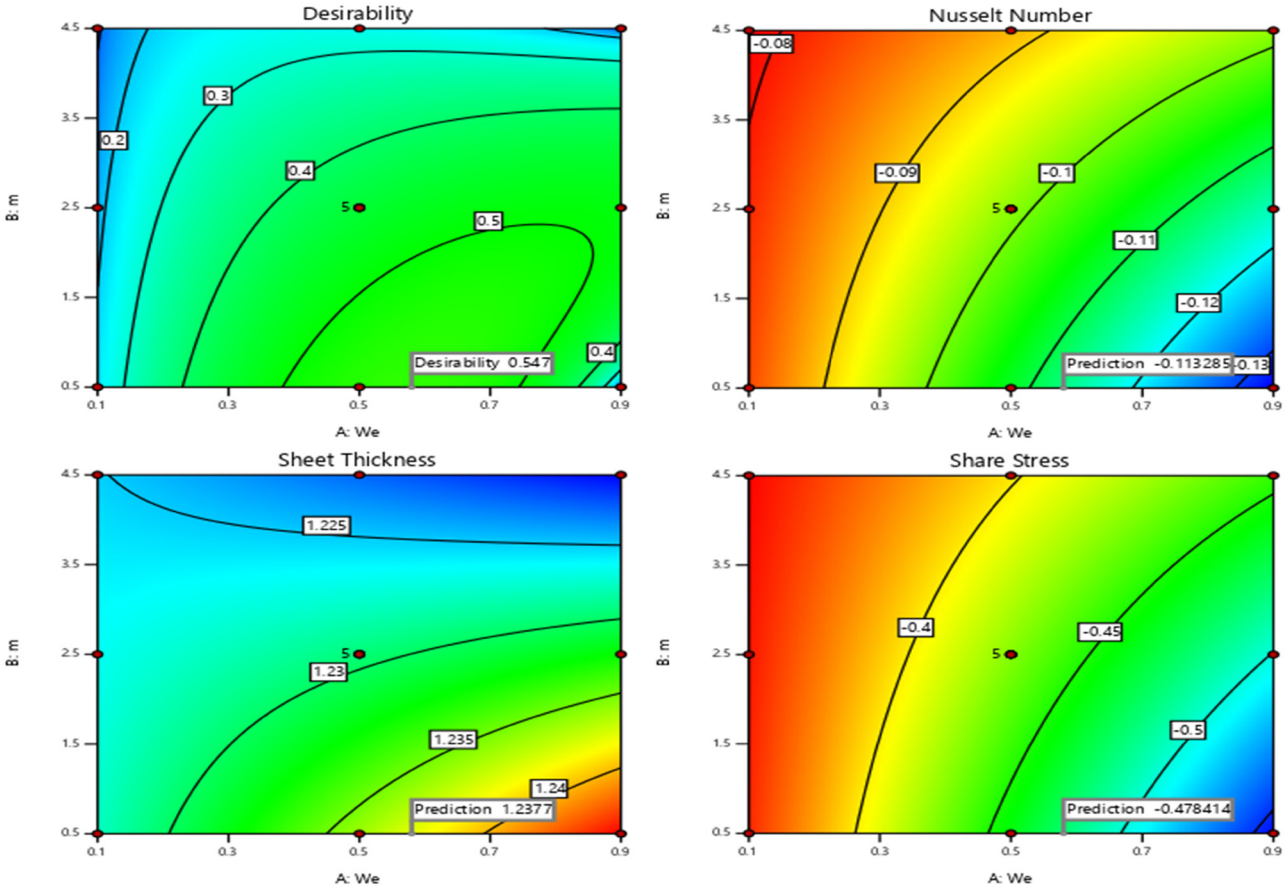

Figure 6: Optimum solution with desirability.

values of the regression models. The regression model is found to be precisely matched with the actual data when the residuals persistently align with or virtually the straight line.

Based on a mathematical framework developed through RSM, response surface plots given in Figure 5(a)–(f) provide a two- and three-dimensional visualization of the relationship in the middle of independent variables along with a specific response variable in the systems. These plots illustrate how variations in the independent variables, represented on the x- and y-axes, influence a particular response variable mapped along the z-axis. Such visualizations are instrumental in identifying optimal conditions and interaction effects within multi-variable processes.

In the calendering process, optimization focuses on achieving key targets: maximizing a particular heat transfer rate (represented by the Nu), $\frac{H}{H_0}$, and minimizing S_{xy}. Minimizing S_{xy} is particularly important, as it reduces the force needed to draw the sheet through the roll gap, enhancing operational efficiency. Simultaneously, maximizing $\frac{H}{H_0}$ and Nu contributes to improved material quality and heat dissipation, which are critical to the product's performance. The optimal factor levels that balance these objectives can be identified using RSM and numerical optimization techniques. RSM facilitates a detailed analysis of interactions and nonlinear effects, enabling the development of a model that minimizes S_{xy} while maximizing Nu and $\frac{H}{H_0}$. This approach uses a "desirability function" to evaluate the combined outcome, where a higher desirability score indicates a more favorable solution across the defined goals. The graphical depiction of this analysis can be observed in Figure 6, and a desirability score of 0.547 was achieved, suggesting a moderate alignment with the targeted objectives. By further fine-tuning the factor levels, the desirability score could potentially increase, yielding an optimal solution with maximized efficiency, product quality, and heat transfer, thereby defining the most favorable conditions for the calendering process.

Residual plots are essential diagnostic tools in regression analysis. They allow for the examination of model assumptions. By analyzing residuals, one can assess the goodness-of-fit of a model and identify potential areas for

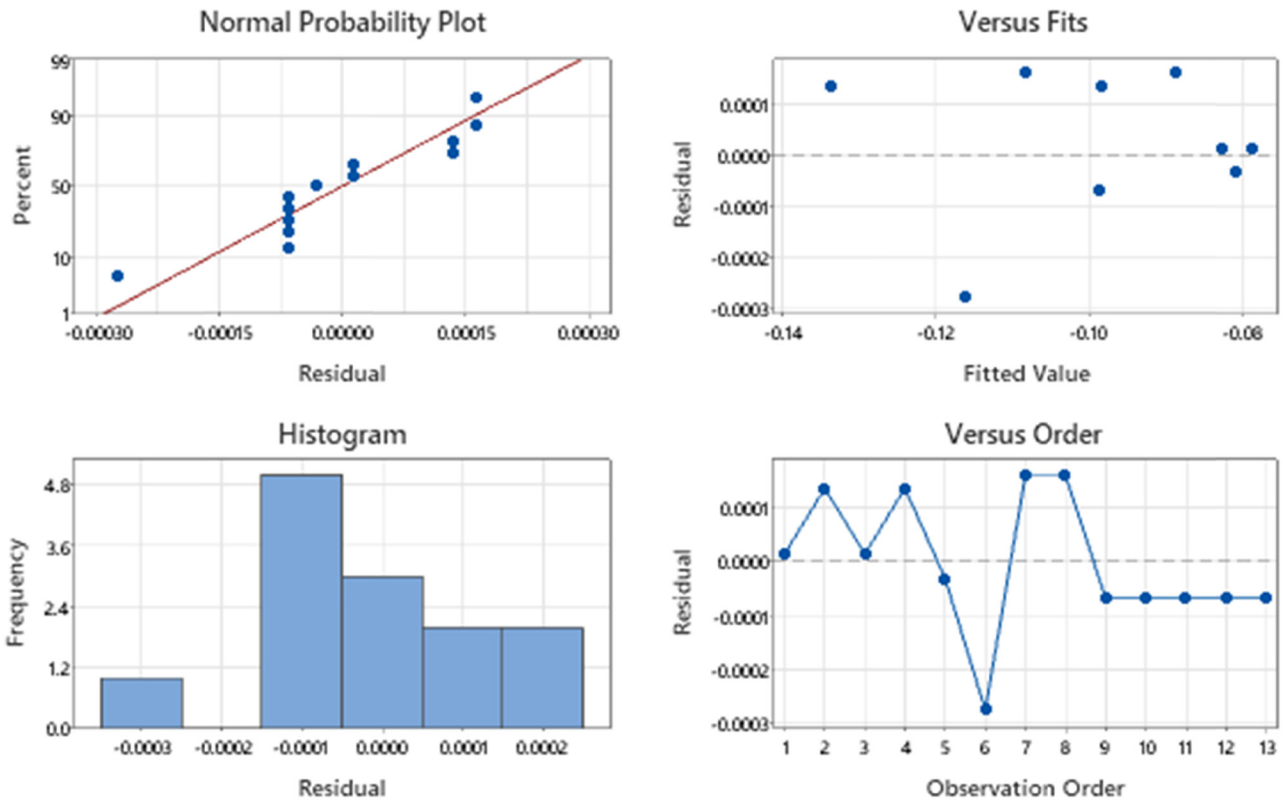

Figure 7: Residual plots for Nusselt number.

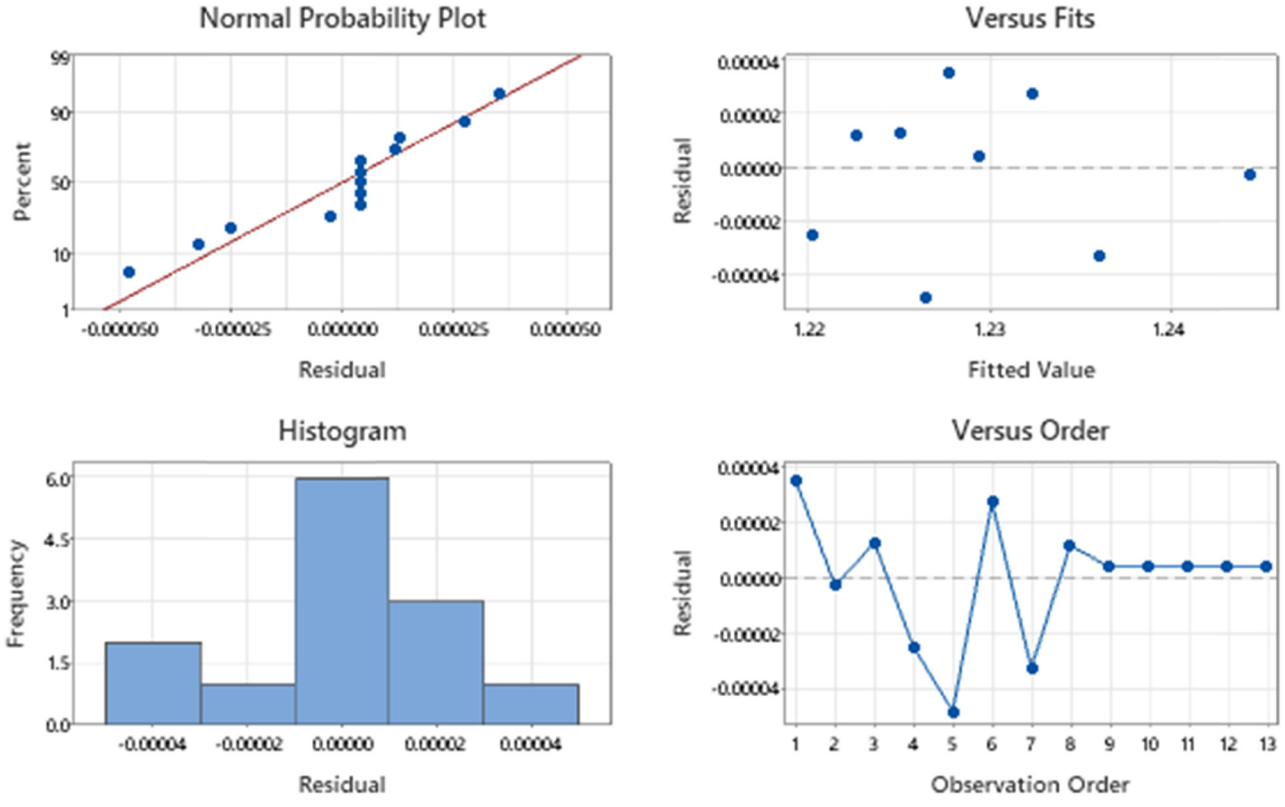

Figure 8: Residual plots for sheet thickness.

improvement or data issues, such as outliers or patterns that the model fails to capture. So, the residual plots for the Nu, $\frac{H}{H_0}$, and S_{xy} are displayed in Figures 7–9. Several key aspects of model performance can be observed. The normal probability plots in all cases show that the residuals generally align well with the red reference line, indicating that the residuals are approximately normally distributed.

Finally, the ANOVA and model summary for Nu, $\frac{H}{H_0}$, and S_{xy} through ANOVA are given in Tables 9–14, independently.

7.3 Sensitivity analysis

Nusselt number, sheet thickness, and shear stress are important in hydrodynamics and calendering processes. Regression Eqs. (52) and (55) are the basis for calculating the sensitivity. The term "sensitivity functions" refers to the restricted derivatives of a certain response variable with regard to the factor variables. They exist as follows:

$$\begin{aligned}\mathrm{Nu} = {} & -0.098604352453103 - 0.017622230318333A \\ & + 0.0098135513666667B + 0.007850841105AB \\ & + 0.00022842028586205B^2,\end{aligned} \tag{54}$$

$$\frac{\partial \mathrm{Nu}}{\partial A} = -0.017622230318333 + 0.007850841105B, \tag{55}$$

$$\begin{aligned}\frac{\partial \mathrm{Nu}}{\partial B} = {} & 0.0098135513666667 + 0.007850841105A \\ & + 0.0004568405718B,\end{aligned} \tag{56}$$

$$\begin{aligned}\frac{H}{H_0} = {} & 1.2294358965517 + 0.0029351666666665A \\ & - 0.0067041666666669B \\ & - 0.0053867499999998AB \\ & + 0.00002436206896561 4A^2 \\ & - 0.0001036379310344B^2,\end{aligned} \tag{57}$$

$$\begin{aligned}\frac{\partial}{\partial A}\left(\frac{H}{H_0}\right) = {} & 0.0029351666666665 \\ & - 0.0053867499999998B \\ & + 0.000048724137 94A,\end{aligned} \tag{58}$$

$$\begin{aligned}\frac{\partial}{\partial B}\left(\frac{H}{H_0}\right) = {} & 0.0067041666666669 \\ & - 0.0053867499999998A,\end{aligned} \tag{59}$$

$$\begin{aligned}S_{xy} = {} & -0.42834923076923 - 0.072526666666667A \\ & + 0.030285B + 0.0263625AB,\end{aligned} \tag{60}$$

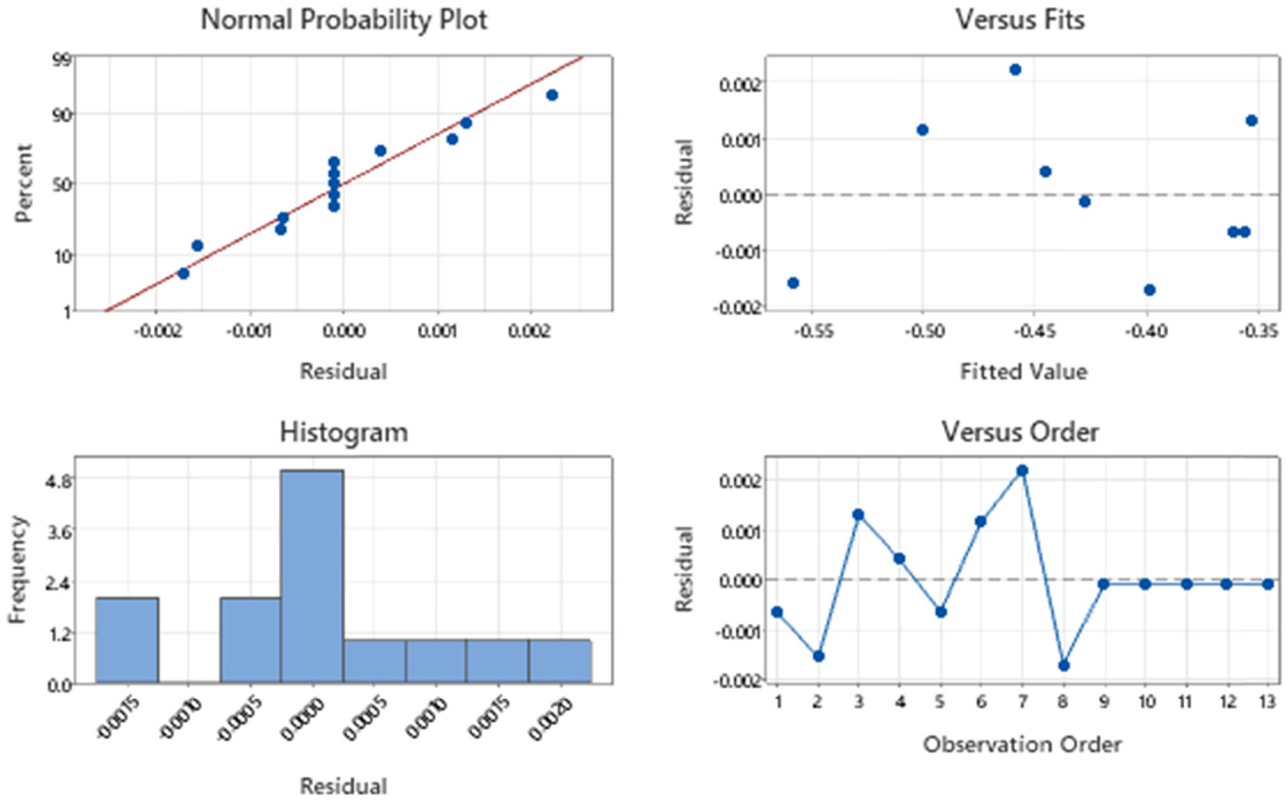

Figure 9: Residual plots for shear stress.

Table 9: ANOVA for Nu

Source	DF	Adj SS	Adj MS	*F*-value	*P*-value
Model	4	0.002688	0.000672	28496.93	0.000
Linear	2	0.002441	0.001221	51765.22	0.000
We	1	0.001863	0.001863	79023.59	0.000
M	1	0.000578	0.000578	24506.84	0.000
Square	1	0.000000	0.000000	1.04	0.338
We*We	1	0.000000	0.000000	1.04	0.338
2-way interaction	1	0.000247	0.000247	10456.25	0.000
We*m	1	0.000247	0.000247	10456.25	0.000
Error	8	0.000000	0.000000		
Lack of fit	4	0.000000	0.000000	*	*
Pure error	4	0.000000	0.000000		
Total	12				

Table 10: Model dummary appropriate to Nu

S	*R*-sq	*R*-sq(adj)	*R*-sq(pred)
0.0001536	99.99%	99.99%	99.97%

$$\frac{\partial S_{xy}}{\partial A} = 0.072526666666667 + 0.0263625B, \tag{61}$$

$$\frac{\partial S_{xy}}{\partial B} = 0.030285 + 0.0263625A, \tag{62}$$

Table 11: ANOVA for sheet thickness

Source	DF	Adj SS	Adj MS	*F*-value	*P*-value
Model	5	0.000437	0.000087	96017.21	0.000
Linear	2	0.000321	0.000161	176338.09	0.000
We	1	0.000052	0.000052	56727.36	0.000
M	1	0.000270	0.000270	295948.82	0.000
Square	2	0.000000	0.000000	16.68	0.002
We*We	1	0.000000	0.000000	1.80	0.222
m*m	1	0.000000	0.000000	32.56	0.001
2-way interaction	1	0.000116	0.000116	127376.52	0.000
We*m	1	0.000116	0.000116	127376.52	0.000
Error	7	0.000000	0.000000		
Lack of fit	3	0.000000	0.000000	*	*
Pure error	4	0.000000	0.000000		
Total	12	0.000437			

Table 12: Model abstract for sheet thickness

S	*R*-sq	*R*-sq(adj)	*R*-sq(pred)
0.0000302	100.00%	100.00%	99.99%

Table 13: ANOVA for shear stress

Source	DF	Adj SS	Adj MS	*F*-value	*P*-value
Model	5	0.039849	0.007970	3872.01	0.000
Linear	2	0.037064	0.018532	9003.54	0.000
We	1	0.031561	0.031561	15333.46	0.000
M	1	0.005503	0.005503	2673.62	0.000
Square	2	0.000005	0.000002	1.18	0.362
We*We	1	0.000001	0.000001	0.41	0.540
m*m	1	0.000002	0.000002	1.09	0.331
2-way interaction	1	0.002780	0.002780	1350.60	0.000
We*m	1	0.002780	0.002780	1350.60	0.000
Error	7	0.000014	0.000002		
Lack of fit	3	0.000014	0.000005	*	*
Pure error	4	0.000000	0.000000		
Total	12	0.039863			

Table 14: Model abstract for shear stress

S	*R*-sq	*R*-sq(adj)	*R*-sq(pred)
0.0014347	99.96%	99.94%	99.64%

where $\frac{\partial \mathrm{Nu}}{\partial A}$. $\frac{\partial \mathrm{Nu}}{\partial B}$, $\frac{\partial}{\partial A}\left(\frac{H}{H_0}\right)$, $\frac{\partial}{\partial B}\left(\frac{H}{H_0}\right)$, $\frac{\partial S_{xy}}{\partial A}$, and $\frac{\partial S_{xy}}{\partial B}$ are a specific sensitivity function. A particular sensitivity of the involved inputs (We, along with m) on quantity produced at distinct levels is described in Table 15. Also, its graphical bar charts given in Figures 10–12 illustrate a particular sensitivity of Nu, $\frac{H}{H_0}$ together with S_{xy}. From these figures, it can be concluded that a positive sensitivity output designate that strengthens the input variable's value enhances the output function's value. Conversely, a negative sensitivity value signifies that increasing the input variable decreases the output function.

8 Results and discussions

This section explains how the involved parameters for an incompressible EP fluid model whose viscosity is temperature-dependent during the calendering process affect the flow velocity, pressure gradient, power input pressure, and streamline graphically. The tables show a certain numeric result for the roll-separating force, leave of point, and the final sheet thickness for the various values of involved parameters.

Physical parameters are involved in the coating process [36].

Table 15: Sensitivity analysis data for Nu, $\frac{H}{H_0}$, and S_{xy}

A:We	B:m	$\frac{\partial \mathrm{Nu}}{\partial A}$	$\frac{\partial \mathrm{Nu}}{\partial B}$	$\frac{\partial}{\partial A}\left(\frac{H}{H_0}\right)$	$\frac{\partial}{\partial B}\left(\frac{H}{H_0}\right)$	$\frac{\partial S_{xy}}{\partial A}$	$\frac{\partial S_{xy}}{\partial B}$
−1	0.5	−0.013697	0.010827	0.0002467	0.010827	−0.059346	0.010827
	2.5	0.002005	0.011741	−0.010527	0.011741	−0.006622	0.011741
	4.5	0.017707	0.012655	−0.0213	0.012655	0.046103	0.012655
0	0.5	−0.013697	0.013967	0.0002662	0.013967	−0.059346	0.013967
	2.5	0.002005	0.014881	−0.010507	0.014881	−0.006622	0.014881
	4.5	0.017707	0.015795	−0.02128	0.015795	0.046103	0.015795
1	0.5	−0.013697	0.017107	0.0002857	0.017107	−0.059346	0.017107
	2.5	0.002005	0.018021	−0.010488	0.018021	−0.006622	0.018021
	4.5	0.017707	0.018935	−0.021261	0.018935	0.046103	0.018935

Parameters	Values	Unit
H_0	$1.2 \times 10^{-4} - 7.6 \times 10^{-6}$	m
U	0.2–5	m s^{-1}
R	0.1...0.15	m
ρ	850...1,200	kg m^3
We	0.1. 0.9	
m	0.5...4.5	
Br	0.1...0.9	

The impact of several parameters on velocity profile $u(y)$, pressure distribution $p(x)$, pressure gradient $\frac{dp}{dx}$, temperature distribution $\theta(y)$, power input (p_w), and Nusselt number (Nu) is shown graphically in Figures 13–20. Figure 13(a) and (b) illustrates the effect of the Weissenberg number (We) on a certain $u(y)$ at the positions $x = -0.5$ and 0, with varying values of We from 0.1 to 0.9, with corresponding changes in the parameter λ, respectively. The We is a dimensionless parameter that distinguishes a viscoelastic fluid's ratio of elastic to viscous forces. From figure, it has been observed that the $u(y)$ increases as We increase. As We increases, λ also increases, indicating that higher elastic effects (associated with larger We) result in increased fluid velocities. The black dotted line labeled "Newtonian" serves as a reference for comparison. It shows the velocity profile characteristic of Newtonian fluids, where viscosity remains constant. The deviation of the non-Newtonian fluid profiles from this baseline clearly demonstrates the impact of the fluid's properties on its flow behavior. Furthermore, comparing the results to the well-understood Newtonian case helps provide validity for the analysis of the non-Newtonian fluid. Figure 14(a) and (b) demonstrates the impact of the viscosity-dependent temperature parameter m on a particular $u(y)$ at the fixed position $x = -0.5$ and $x = 0$ in the process under consideration. The parameter m represents the domination of temperature on the fluid's viscosity, with the graph illustrating profiles for various values of m ranging from 0.5 to 4.5, each associated with a different value of λ.

Figure 14(a) illustrates the significant impact of the temperature-dependent viscosity parameter m on the velocity profile $u(y)$ and leave distance λ during calendering. As m increases from 0.5 to 4.5, the fluid velocity systematically decreases. This indicates that a higher "m" value, signifying greater sensitivity of viscosity to temperature

Table 16: Effect of We on leave-off distance, final sheet thickness, and roll separation force

We	λ	$\frac{H}{H_0}$	F
0.1	0.47752	1.2280	−6.754281
0.2	0.47992	1.2303	−6.756111
0.3	0.48232	1.2326	−6.757941
0.4	0.48472	1.2349	−6.759770
0.5	0.48712	1.2372	−6.761599
0.6	0.48952	1.2396	−6.763428
0.7	0.49192	1.2419	−6.765262
0.8	0.49432	1.2443	−6.767085
0.9	0.49672	1.2467	−6.768913

Table 17: Effect of m on leave-off distance, final sheet thickness, and roll separation force

m	λ	$\frac{H}{H_0}$	F
0.5	0.48578	1.2359	−6.76099
1	0.48411	1.2343	−6.75727
1.5	0.48242	1.2327	−6.75761
2	0.48071	1.2310	−6.75787
2.5	0.47897	1.2294	−6.75392
3	0.47722	1.2277	−6.75403
3.5	0.47545	1.2260	−6.75404
4	0.47365	1.2243	−6.74988
4.5	0.47183	1.2226	−6.74973

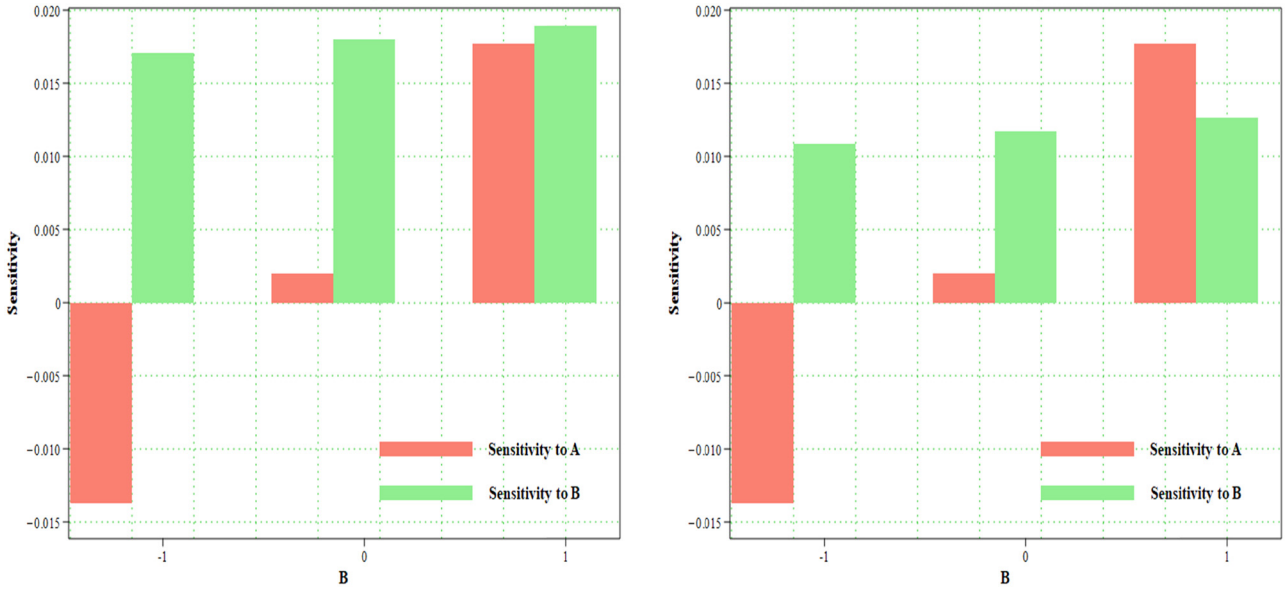

Figure 10: Sensitivity analysis of Nu at $A = -1$ and at $A = 1$, respectively.

changes, leads to effectively higher fluid viscosity and slower fluid flow. Specifically, low m values (*e.g.*, 0.5) correspond to less temperature-sensitive fluids, allowing for higher flow velocities. Conversely, increasing "m" drastically increases viscosity in response to temperature variations, resulting in greater internal resistance and reduced flow rates. This reduction in velocity is directly linked to a decrease in the λ, the point of material detachment from the roll. Similarly, Figure 14(b) depicts the $u(y)$ at $x = 0$, the midpoint between the calendering rollers; with various values of the m, maximum $u(y)$ is observed, indicating that the fluid moves more uniformly in this region. This position represents the midpoint of the flow, where the shear rates are relatively lower compared to the edges of the calendering system. A similar trend can be perceived from Figure 15(a) and (b) for a certain increasing value of Br.

The pressure gradient $\frac{dp}{dx}$ and the pressure profile $(p(x))$ are crucial factors in a certain calendering process

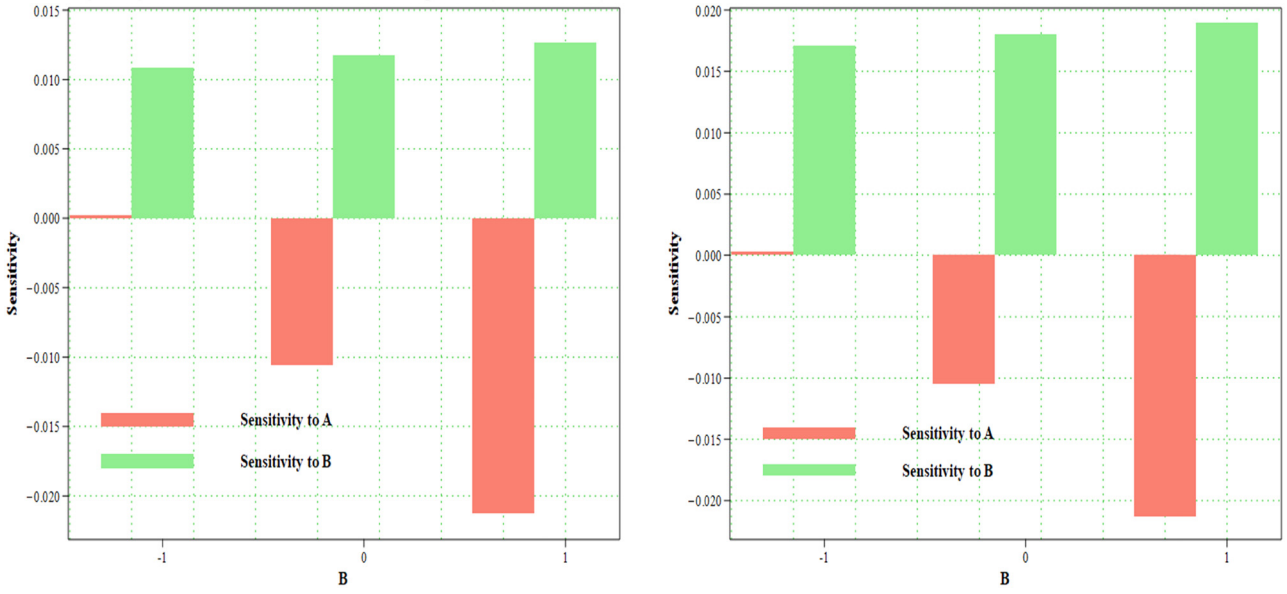

Figure 11: Sensitivity analysis of $\frac{H}{H_0}$ at $A = -1$ and at $A = 1$, respectively.

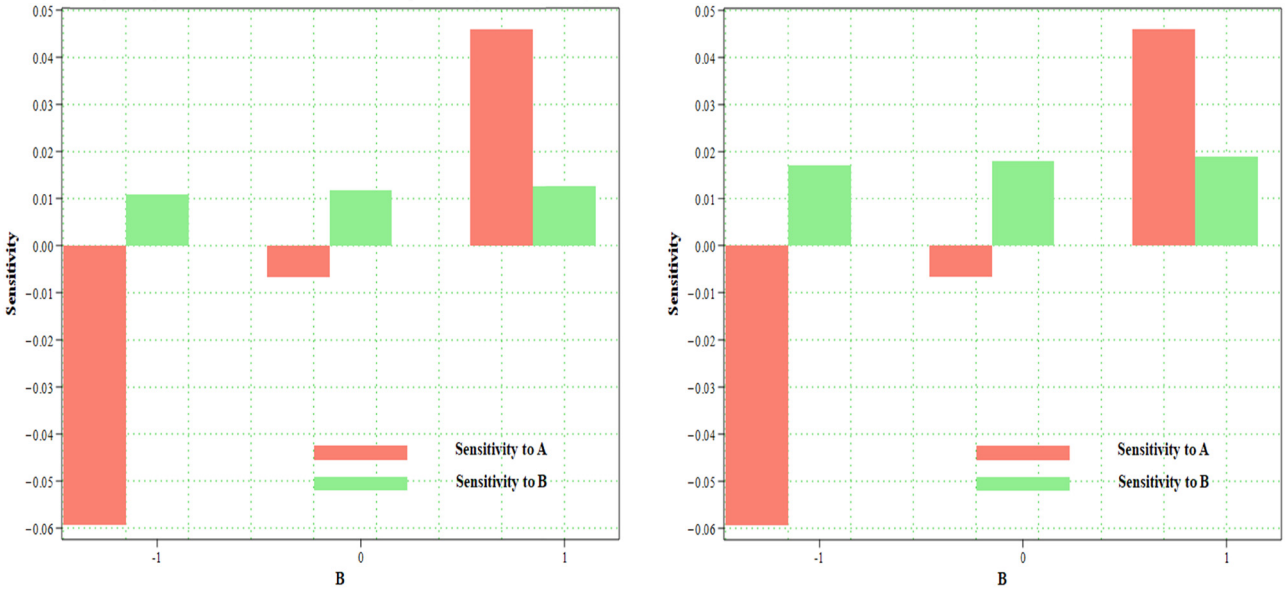

Figure 12: Sensitivity analysis of S_{xy} at $A = -1$ and at $A = 1$, respectively.

of EP fluids. The $\frac{dp}{dx}$, which is the outlay of interchange of $p(x)$ with respect to an interval x along the roll gap, represents the driving force for fluid flow. So, Figure 16(a) and (b) shows the impact of emerging parameters on $\frac{dp}{dx}$, whereas Figure 16(a) illustrates the effect of the We on the $\frac{dp}{dx}$ along the roll gap x. It is observed that the $\frac{dp}{dx}$ exhibits symmetric behavior around the nip region at $x = 0$, where the rollers are in closest contact. The $\frac{dp}{dx}$ profiles exhibit symmetric behavior around the nip region ($x = 0$). As it moves away from the nip region, the $\frac{dp}{dx}$ increases symmetrically and eventually turns to zero at the attachment and detachment points, where the fluid exits the rollers. Also, as the We increases, the magnitude of the $\frac{dp}{dx}$ increases. With an increase in $\frac{dp}{dx}$, the amount We is primarily due to the enhanced elastic effects in the fluid. At higher We, the elastic forces become more dominant than the viscous forces, leading to a greater resistance to

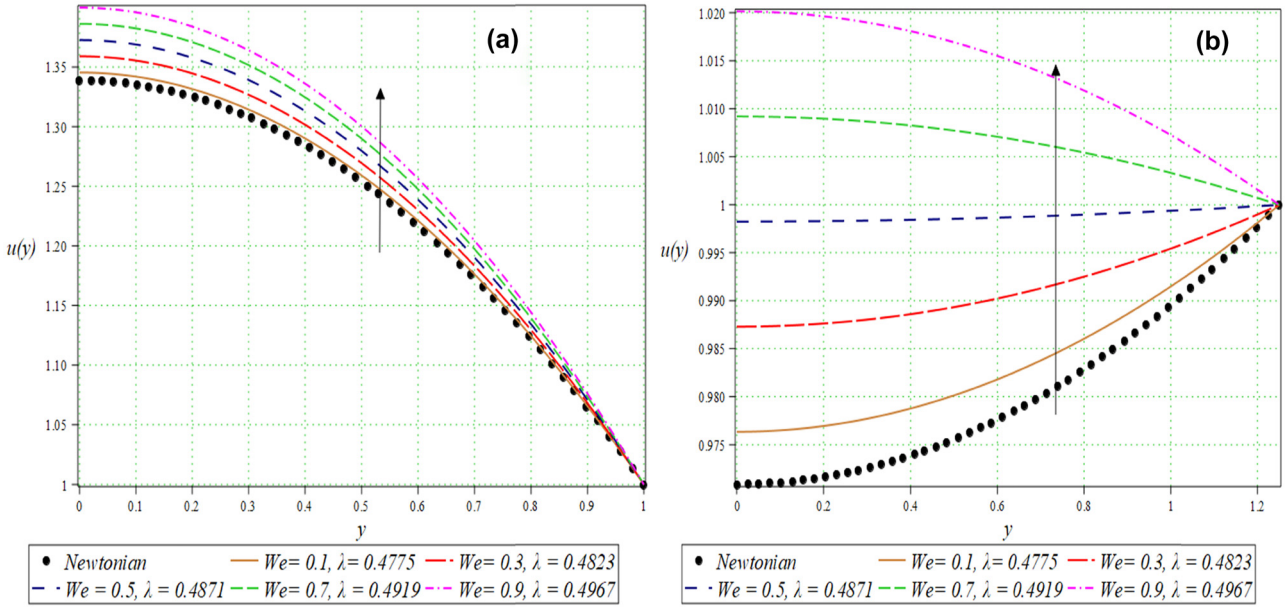

Figure 13: $u(y)$ for distinct values of We at (a) $x = -0.5$ and (b) $x = 0$.

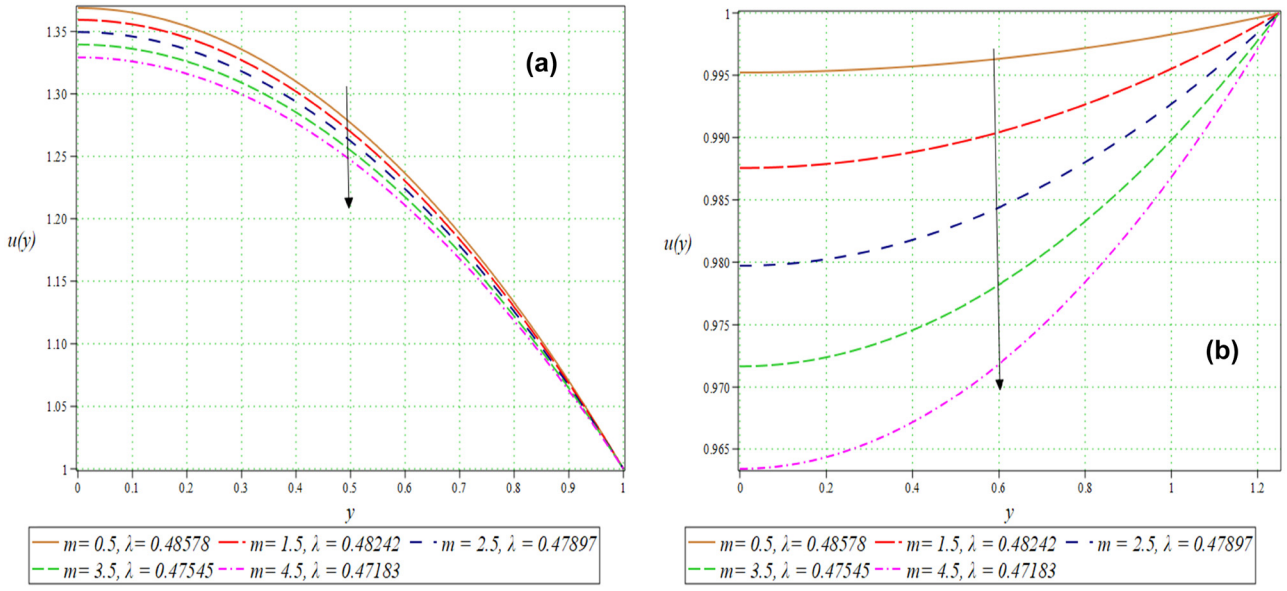

Figure 14: $u(y)$ for distinct values of m at (a) $x = -0.5$ and (b) $x = 0$.

flow and a higher-pressure buildup, suggesting a stronger driving force for fluid flow between the rolls. Moreover, it is translucent from Figure 16(b) that a particular incompatible trend has been detected for increasing m value as compared to We.

The pressure profile, which is the variation of pressure across the roll gap, is influenced by the $\frac{dp}{dx}$, and fluid properties are shown in Figure 17(a) and (b). The consequence of We on $p(x)$ along the roller length during the calendering process is illustrated in Figure 17(a). From figure, it can be observed that the We varies from 0.1 to 0.9, with each profile corresponding to a specific value of We and its associated leave distance λ. The pressure profile exhibits a peak just before the nip region ($x = 0$), after which it sharply declines. This peak position is physically intuitive, as the maximum pressure is needed to force the fluid through the narrowest part of the channel, where the rollers are closest together. As We increases, the pressure

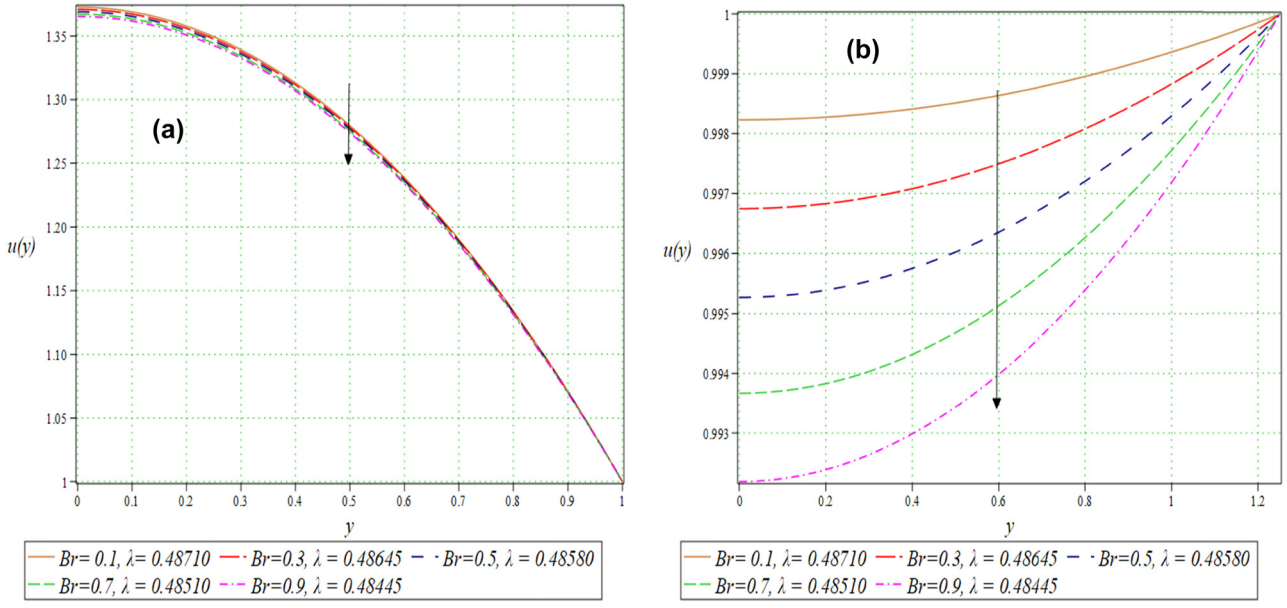

Figure 15: $u(y)$ for distinct values of Br at (a) $x = -0.5$ and (b) $x = 0$.

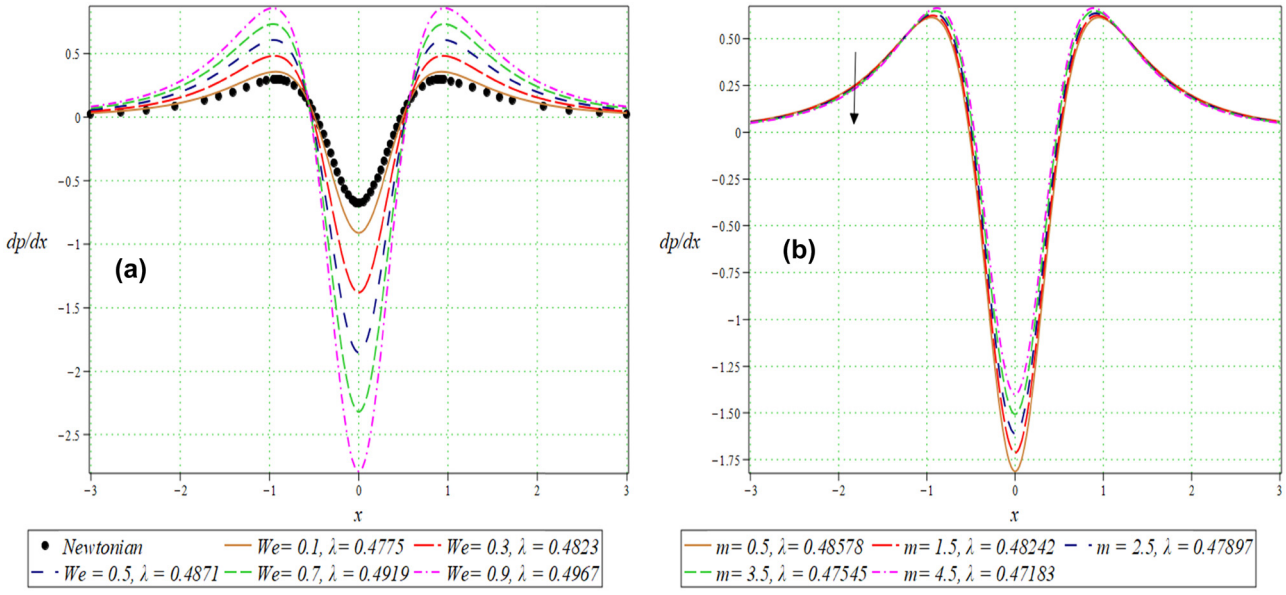

Figure 16: $\frac{dp}{dx}$ against x for distinct values of (a) We and (b) m.

curves rise, especially around the peak, indicating higher pressure build-up due to enhanced elastic effects, whereas the decreasing trend has been observed for the increasing value of m. This behavior arises because higher m values correspond to a stronger reduction in viscosity with increasing temperature. Both plots include a reference Newtonian case (black dots), which serves as a benchmark to assess the behavior of non-Newtonian fluids under varying physical conditions.

The temperature profile $\theta(y)$ plays a crucial role in the calendering process for variable viscosity fluids, as it significantly impacts the fluid's rheological properties, such as viscosity and flow behavior. In calendering, temperature variations can cause the fluid's viscosity to change dynamically. A higher temperature typically reduces the fluid's viscosity, making it easier for the fluid to flow and spread evenly, which is crucial for achieving uniform coating thickness. Figures 18(a) and (b) and 19(b) show

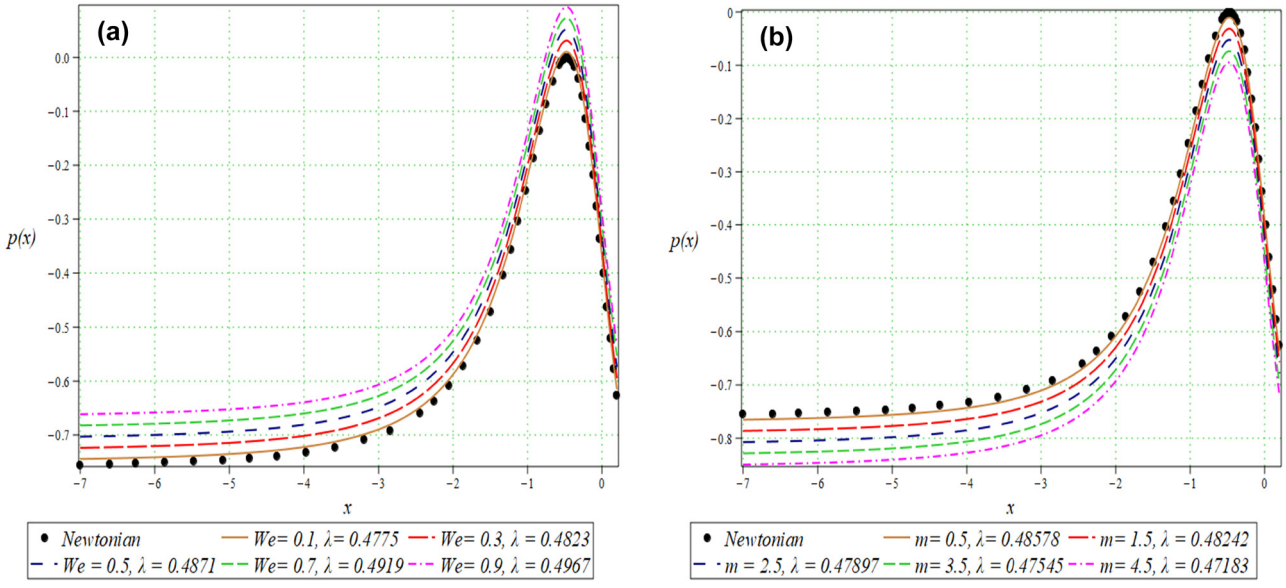

Figure 17: $p(x)$ against x for distinct values of (a) We and (b) m.

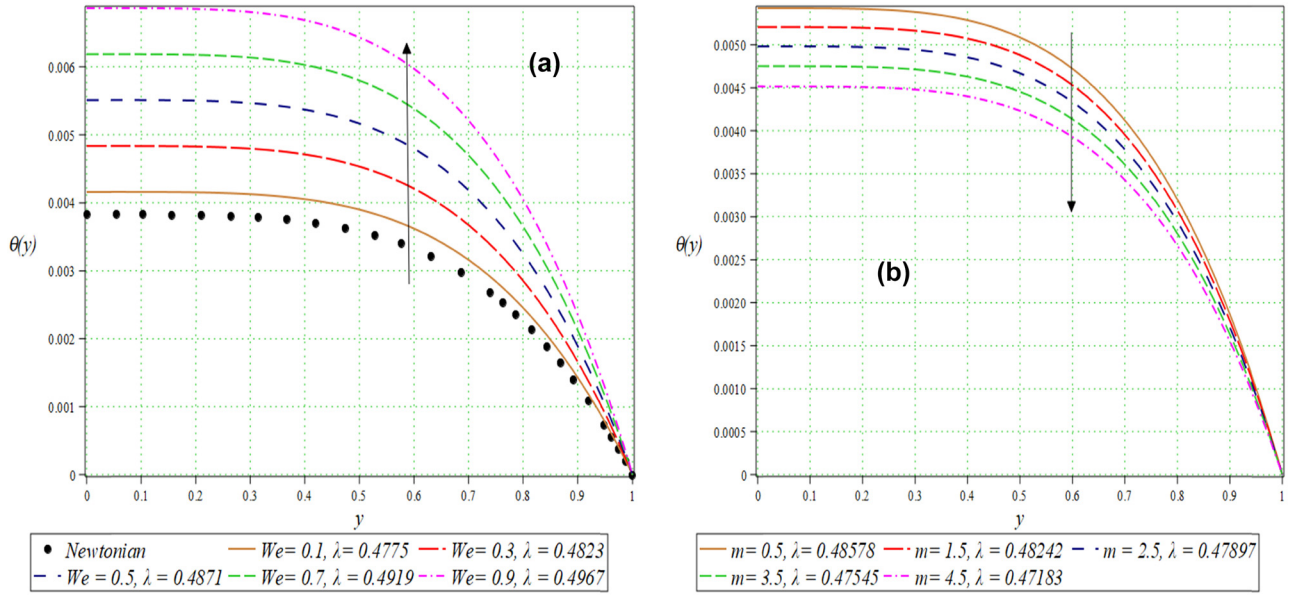

Figure 18: Temperature distribution opposed to y for dissimilar values of (a) We and (b) m.

the impact of various emerging parameters on $\theta(y)$. The x-axis is elected by the dimensionless distance along the calender, and the y-axis is elected by the dimensionless temperature. Figure 18(a) investigates the influence of the We – a dimensionless parameter characterizing the elastic properties of the fluid on temperature against y within the flow domain. The graph includes multiple curves corresponding to We = 0.1, 0.3, 0.5, 0.7, and 0.9, as well as a black dotted line labeled "Newtonian" that serves as a reference for a Newtonian fluid (a fluid with constant viscosity). There is also an upward arrow shown on the graph, pointing from the lower lines toward the upper lines. This arrow, along with the legend at the bottom, clearly indicates that as the We increases, the corresponding outcomes for temperature shift upward. Physically, it means that as We increases, it indicates a stronger dominance of elastic effects in the fluid behavior. These elastic effects cause the fluid particles to stretch and store

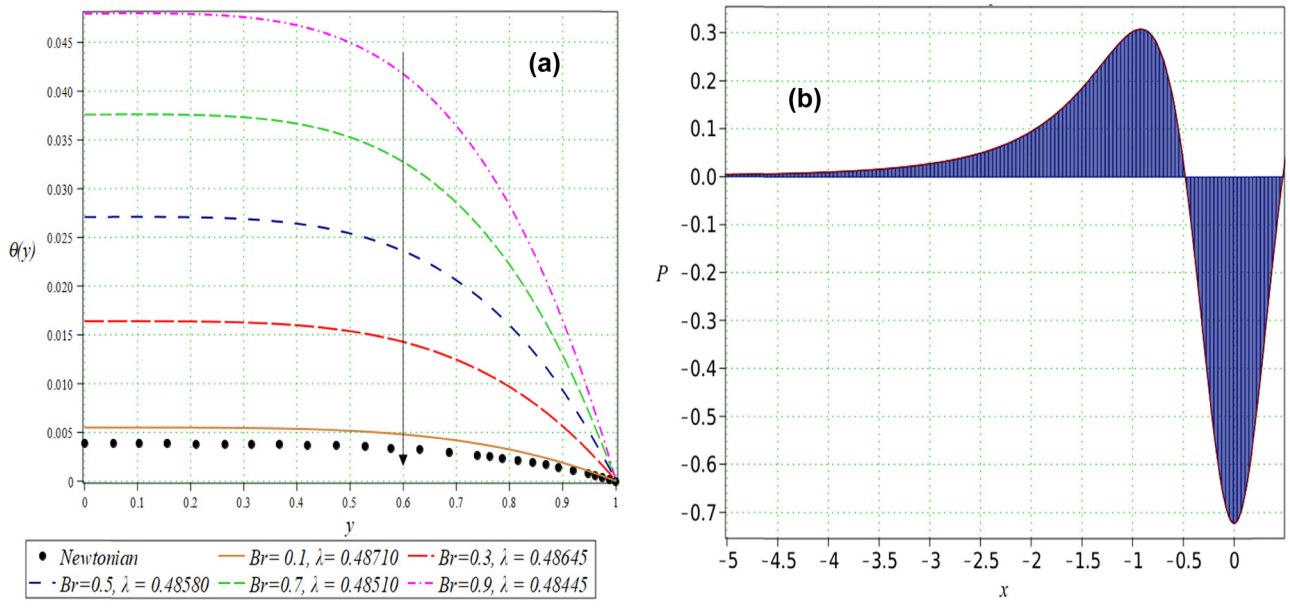

Figure 19: Temperature distribution opposed to y for various values of (a) We and (b) p_w.

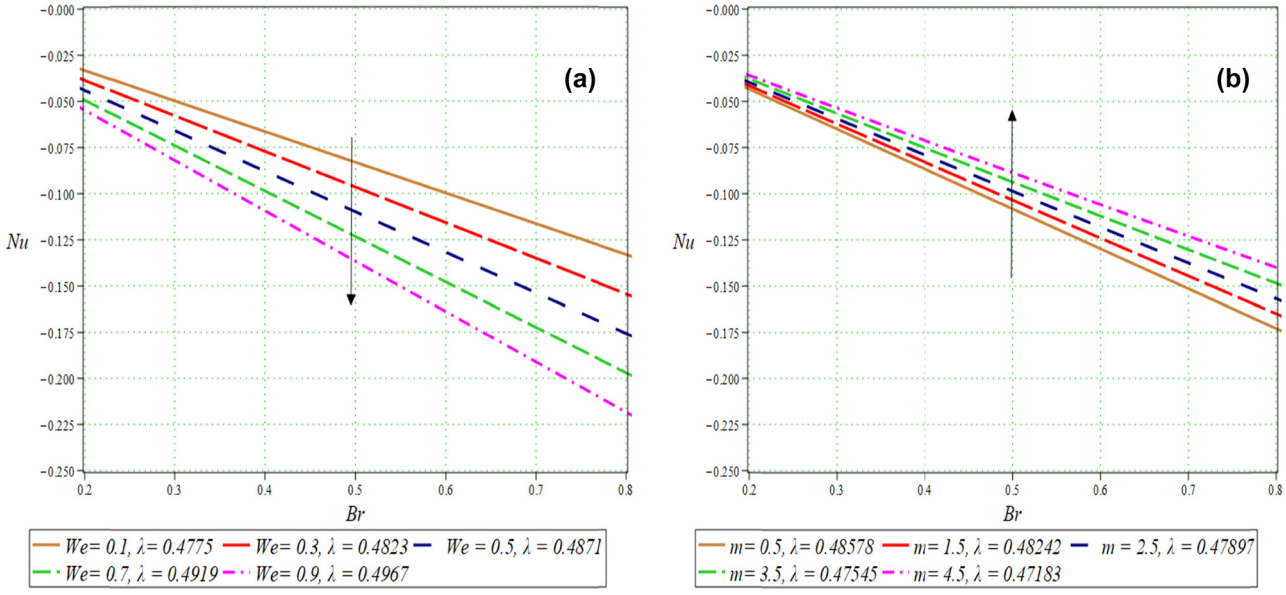

Figure 20: Nu for different values of (a) We and (b) m.

deformation energy, which is then gradually released during flow. This process generates additional internal stresses, which contribute to dissipative heating – a mechanism where mechanical energy is converted into thermal energy within the fluid. As a result, the conversion of elastic energy into heat leads to a rise in the fluid temperature. A similar trend can be witnessed from Figure 19(a) for Br. In contrast, the illustration of the influence of the m (from the Reynolds model of viscosity) on the temperature profile $\theta(y)$ is shown in Figure 18(b). The figure shows that as m increases from 0.5 to 4.5, the temperature profile exhibits a noticeable decreasing trend. As m increases, the temperature profile progressively lowers, indicating that the fluid's viscosity is more strongly influenced by temperature. This reduction in temperature suggests less heat generation due to internal friction or viscous dissipation, as the fluid becomes more responsive to temperature variations. This trend highlights the crucial role of m in controlling the thermal behavior of the fluid. Therefore, m is essential for managing the temperature distribution and optimizing the performance of the calendering process for variable viscosity fluids. Also, the p_w is displayed in Figure 19(b).

In Figure 20(a), we observe the consequence of increasing a specific We on a given Nu. The graph shows that as the We rises, the Nu also increases. This implies that higher elastic effects (increased We) lead to enhanced heat transfer in the system. Physically, this suggests that as the fluid's elasticity grows, the flow becomes more capable of dissipating thermal energy, which is reflected in the rising Nu. Additionally, a particular detachment point λ increases with the We, further indicating that the elastic forces impact both the flow separation and the heat transfer process. Figure 20(b) highlights the influence of the m on the Nu. Here, it is evident that as m increases, the Nu decreases. This shows that as the temperature dependence of the viscosity becomes stronger (with higher m), the heat transfer rate drops. Moreover, the numeric outcome for the impact of the We on several key parameters, inclusive of a certain contingent point (λ), $\frac{H}{H_0}$, and the force separating the rolls, is illustrated in Table 16. The results indicate that as the We increases, both the λ and $\frac{H}{H_0}$ rise while the roll-separating force decreases. In Table 17, the influence of the m is analyzed. It is evident that as the m increases, both the λ and $\frac{H}{H_0}$ show a decreasing trend.

9 Conclusions

This study presents a comprehensive theoretical investigation into the influence of various factors on the temperature-dependent viscosity of an Eyring–Powell fluid flowing between two equally sized rolls rotating at identical speeds in a calendering process. By applying an appropriate transformation, the dimensional momentum and energy-governing equations were converted into a non-dimensional form and simplified using the lubrication approximation theory. The resulting nonlinear ordinary differential equations were analytically solved using a perturbation

method. The accuracy of the RSM approach was found to be approximately 99%, which was employed to generate 3D surface plots and 2D contour plots. The fluid flow characteristics, analyzed in terms of key parameters, were presented through tables and graphs, offering valuable insights.

The study revealed that the maximum fluid velocity occurs at the mid-region of the calender gap. An increase in the viscosity parameter was observed to reduce the detachment point, sheet thickness, pressure gradient, and pressure profile. Conversely, an increase in the Brinkman number enhanced the velocity profile while decreasing the temperature distribution. Additionally, the viscosity parameter significantly influenced the Nusselt number, thereby impacting heat transfer efficiency.

These findings enhance the understanding of heat transfer and flow dynamics in the calendering process of Eyring–Powell fluids, providing practical insights for optimizing industrial applications. The study also lays a solid foundation for future research in this area.

Acknowledgments: This work was supported by the Deanship of Scientific Research, Vice Presidency for Graduate Studies and Scientific Research, King Faisal University, Saudi Arabia (Grant No. 252105). Also, this research was supported by the Talent Project of Tianchi Young-Doctoral Program in Xinjiang Uygur Autonomous Region of China (Grant No. 51052401510).

Funding information: This work was supported by the Deanship of Scientific Research, Vice Presidency for Graduate Studies and Scientific Research, King Faisal University, Saudi Arabia (Grant No. 252105).

Author contributions: The idea was created and integrated into a mathematical model by F.A. & M.Z.; F.A. solved the problem; F.A. and M.F. wrote the manuscript; B.S., N.A.T., F.A. and A.A.F. highlighted the physics involved in the problem and added to the discussion of it; S.S.K.R., F.A., and M.W.A. reviewed, edited, and helped with the English corrections. All authors have accepted responsibility for the entire content of this manuscript and approved its submission.

Conflict of interest: The authors state no conflict of interest.

Data availability statement: Data sharing is not applicable to this article as no datasets were generated or analyzed during the current study.

References

[1] Javed M, Akram R, Nazeer M, Ghaffari A. Heat transfer analysis of the non-Newtonian polymer in the calendering process with slip effects. Int J Mod Phys B. 2024;38:2450105.
[2] Ardichvili G. An attempt at a rational determination of the ambering of calender rolls. Kautschuk. 1938;14:23–5.
[3] Paslay P. Calendering of a viscoelastic material. J Appl Mech. 1957;24(4):602–8.
[4] Bergen J, Scott Jr G. Pressure distribution in the calendering of plastic materials. J Appl Mech. 1951;18(1):101–6.
[5] Gaskell R. The calendering of plastic materials. J Appl Mech. 1950;17(3):334–6.
[6] Kiparissides C, Vlachopoulos J. Finite element analysis of calendering. Polym Eng Sci. 1976;16:712–9.
[7] Tadmor Z, Gogos CG. Principles of polymer processing. Hoboken, New Jersey, USA: John Wiley & Sons; 2013.
[8] Brazinsky I, Cosway H, Valle Jr C, Jones RC, Story V. A theoretical study of liquid-film spread heights in the calendering of Newtonian and power law fluids. J Appl Polym Sci. 1970;14:2771–84.
[9] Alston Jr WW, Astill KN. An analysis for the calendering of non-Newtonian fluids. J Appl Polym Sci. 1973;17:3157–74.
[10] Middleman S. Fundamentals of polymer processing. New York: McGraw-Hill; 1977.
[11] Soong DS. Polymer processing. Chem Eng Educ. 1981;15:204–7.
[12] Zheng R, Tanner R. A numerical analysis of calendering. J Non-Newtonian Fluid Mech. 1988;28:149–70.
[13] Mitsoulis E, Vlachopoulos J, Mirza F. Calendering analysis without the lubrication approximation. Polym Eng Sci. 1985;25:6–18.
[14] Arcos J, Méndez F, Bautista O. Effect of temperature-dependent consistency index on the exiting sheet thickness in the calendering of power-law fluids. Int J Heat Mass Transf. 2011;54:3979–86.
[15] Sofou S, Mitsoulis E. Calendering of pseudoplastic and viscoplastic sheets of finite thickness. J Plastic Film Sheeting. 2004;20:185–222.
[16] Hatzikiriakos SG. Professor E. Mitsoulis's contributions to rheology and computational non-Newtonian fluid mechanics. J Non-Newtonian Fluid Mech. 2023;311:104973.
[17] Arcos J, Bautista O, Méndez F, Bautista E. Sensitivity of calendered thickness to temperature variations for Newtonian fluids. Eur J Mech-B/Fluids. 2012;36:97–103.
[18] Zahid M, Rana M, Siddiqui A, Haroon T. Modeling of non-isothermal flow of a magnetohydrodynamic, viscoplastic fluid during calendering. J Plastic Film Sheeting. 2016;32:74–96.
[19] Hernández A, Arcos J, Méndez F, Bautista O. Effect of pressure-dependent viscosity on the exiting sheet thickness in the calendering of Newtonian fluids. Appl Math Model. 2013;37:6952–63.
[20] Arcos J, Bautista O, Méndez F, Bautista E. Theoretical analysis of the calendered exiting thickness of viscoelastic sheets. J Non-Newtonian Fluid Mech. 2012;177:29–36.
[21] Ali N, Javed MA, Sajid M. Theoretical analysis of the exiting thickness of sheets in the calendering of FENE-P fluid. J Non-Newtonian Fluid Mech. 2015;225:28–36.
[22] Calcagno B, Hart K, Crone W. Calendering of metal/polymer composites: an analytical formulation. Mech Mater. 2016;93:257–72.
[23] Zahid M, Ali F, Souayeh B, Khan MT. Influence of variable viscosity on existing sheet thickness in the calendering of non-isothermal viscoelastic materials. Open Phys. 2024;22:20240023.

[24] Ali N, Javed MA, Atif HM. Non-isothermal analysis of calendering using couple stress fluid. J Plastic Film Sheeting. 2018;34:358–81.
[25] Ali F, Hou Y, Zahid M, Rana MA. Mathematical analysis of pseudoplastic polymers during reverse roll-coating. Polymers. 2020;12:2285.
[26] Akinshilo AT, Olaye O. On the analysis of the Erying Powell model based fluid flow in a pipe with temperature dependent viscosity and internal heat generation. J King Saud Univ-Eng Sci. 2019;31:271–9.
[27] Ali F, Narasimhamurthy S, Hegde S, Usman M. Temperature-dependent viscosity analysis of Powell–Eyring fluid model during a roll-over web coating process. Polymers. 2024;16:1723.
[28] Darbari B, Rashidi S, Abolfazli Esfahani J. Sensitivity analysis of entropy generation in nanofluid flow inside a channel by response surface methodology. Entropy. 2016;18:52.
[29] Javed MA, Ali N, Sajid M. A theoretical analysis of the calendering of Ellis fluid. J Plastic Film Sheeting. 2017;33:207–26.
[30] Javed MA, Ali N, Arshad S, Nawaz S, Ghaffari A. Theoretical investigation of a fluid model in calendering process involving slip at the upper roll surface. ZAMM-J Appl Math Mech/Z Angew Math Mech. 2023;103:e202100406.
[31] Abbas Z, Khaliq S. Calendering analysis of non-isothermal viscous nanofluid containing Cu-water nanoparticles using two counter-rotating rolls. J Plastic Film Sheeting. 2021;37:182–204.
[32] Javed MA, Asghar Z, Atif HM, Nisar M. A computational study of the calendering processes using Oldroyd 8-constant fluid with slip effects. Polym Polym Compos. 2023;31:09673911231202888.
[33] Patel M, Timol M. Numerical treatment of Powell–Eyring fluid flow using method of satisfaction of asymptotic boundary conditions (MSABC). Appl Numer Math. 2009;59:2584–92.
[34] Hussain F, Subia GS, Nazeer M, Ghafar M, Ali Z, Hussain A. Simultaneous effects of Brownian motion and thermophoretic force on Eyring–Powell fluid through porous geometry. Z Naturforsch A. 2021;76:569–80.
[35] Nazeer M, Ahmad F, Saeed M, Saleem A, Naveed S, Akram Z. Numerical solution for flow of a Eyring–Powell fluid in a pipe with prescribed surface temperature. J Braz Soc Mech Sci Eng. 2019;41:518.
[36] Abbas Z, Khaliq S. Numerical study of non-isothermal analysis of exiting sheet thickness in the calendering of micropolar-Casson fluid. J Plastic Film Sheeting. 2022;38:105–29.